Jeong
Journal of Analytical Science and Technology (2024) 15:10
https://doi.org/10.1186/s40543-024-00425-5

Journal of Analytical Science and Technology

REVIEW

Open Access

Microanalysis and mineralogy of Asian and Saharan dust

Gi Young Jeong[1*]

Abstract

Mineral dust is transported over long distances from desert sources, interacting with Earth environments. The mineralogy and microstructures of individual dust particles are required to understand the interactions. Here, I summarize recent findings from electron microscopy of dust particles, focusing on Asian and Saharan dust. Dust particles are heterogeneous mixtures of clay and nonclay minerals. Clay minerals account for more than half of the mass of mineral dust. Fine grains of clay minerals form their own aggregates, coat coarse nonclay minerals, or become a matrix of composite particles. The most abundant clay minerals are illite–smectite series clay minerals (ISCMs) dominated by illite and interstratified illite–smectite. Saharan dust is distinct from Asian dust by the high contents of palygorskite and hexagonal kaolinite. Common nonclay silicates are quartz, K-feldspar, and Na-rich plagioclase. Amorphous silica is associated with clays in Saharan dust. Calcite occurs as nanofibers as well as coarse grains, reacting with atmospheric acids to precipitate gypsum. The submicron grains of iron oxides and titanium oxides are scattered through the fine matrix of dust particles. ISCMs, chlorite, biotite, and iron oxides are iron carriers to remote ecosystems. The shapes of dust particles approximate ellipsoids whose aspect ratios increase with clay contents. The mineralogical classification of dust particles has led to the determination of the bulk mineral composition of a very small quantity of samples. The constituent mineralogy of dust particles is discussed in an environmental context with a brief introduction of the geological backgrounds of the minerals in their source areas.

Keywords Dust, Mineralogy, Microstructure, TEM, SEM

Introduction

Mineral dust from arid sources migrates long distances across the oceans, reaching other continents (Prospero 1996; Goudie and Middleton 2001; McKendry et al. 2008; Uno et al. 2009). During transport, mineral dust interacts with electromagnetic radiation, atmospheric gases, liquids, and pollutants and finally becomes terrestrial and marine sediments after deposition. The effect of mineral dust on Earth environments has attracted the attention of broad disciplines, including atmospheric chemistry (Seinfeld et al. 2004; Sullivan et al. 2009; Karydis et al. 2017), climate change (Harrison et al. 2001; Cruz et al. 2021), geochemistry (Pettke et al. 2000; Muhs et al. 2018), Quaternary geology (Porter 2001; Jeong et al. 2013), air pollution (Meskhidze et al. 2005), remote sensing (Sokolik and Toon 1999), marine productivity (Martin and Fitzwater 1988; Myriokefalitakis et al. 2018), and public health (Kwon et al. 2002; Middleton et al. 2008).

Mineral dust cannot be simply defined by size distribution and chemical composition. Many important properties in the Earth environment are related to the mineralogical nature of mineral dust. Pristine dust particles are heterogeneous mixtures of mineral grains of varying sizes, equivalent to a soil fragment blown to high altitude (Kandler et al. 2007; Jeong 2008; Jeong and Nousiainen 2014; Jeong et al. 2016) (hereafter, grain is termed a solid object making up a dust particle). Most chemical elements in dust occupy crystallographic sites

*Correspondence:
Gi Young Jeong
jearth@anu.ac.kr
[1] Department of Earth and Environmental Sciences, Andong National University, Andong 36729, Republic of Korea

in minerals. Each mineral has an inherent crystal structure and a chemical composition often varying in a limited range, resulting in characteristic physical and chemical properties: color, size, morphology, hardness, density, refractive indices, magnetic properties, solubility, specific surface area, surface charge, and adsorption (Klein and Hurlbut 1993; Nesse 2012). The properties and mixing of the constituent minerals of dust particles affect the interactions between mineral dust and Earth environments.

Dust research has increasingly recognized the roles of mineralogical properties in the Earth environment. The modeling of light–particle interactions requires knowledge of the mineral composition, external morphology, and internal microstructures of individual dust particles (Sokolik and Toon 1999; Kandler et al. 2007; Nousiainen 2009; Kemppinen et al. 2015; Li and Sokolik 2018; Conny et al. 2019; Huang et al. 2019; Di Biagio et al. 2020; Conny et al. 2020). The bioavailability of iron in mineral dust is dependent on the solubility of host minerals (Cwiertny et al. 2008; Journet et al. 2008; Myriokefalitakis et al. 2018). The reactivity of calcite is significantly higher than that of other minerals (Laskin et al. 2005). The surfaces of certain minerals are more effective in ice nucleation, inducing the formation of high-altitude clouds (Atkinson et al. 2013). Eolian mineral grains dominate the fine fraction of silty soils and sediments along the migration path of dust (Rex et al. 1969; Mizota et al. 1991; Jeong et al. 2013). Thus, the mineralogy of dust particles broadly influences the Earth's environment. Modeling the effect of mineral dust on the environment requires a consistent data set of mineral composition and properties (Claquin et al. 1999; Scanza et al. 2015), which has not yet been established due to the very low quantity of samples, the lack of systematic analyses and interpretation, and the poor mineralogical information on the soils and sediments in desert sources. Thus, we need to continue the build-up of reliable and consistent mineralogical data sets.

The major analytical tools for investigating individual dust particles include electron microbeam methods such as scanning electron microscopy (SEM) and transmission electron microscopy (TEM). In particular, the application of focused ion beam (FIB) technique to sample preparation has significantly advanced the microanalysis of tiny dust particles (Conny 2013; Jeong and Nousiainen 2014; Jeong et al. 2016). The combined applications of electron microscopy, electron diffraction, energy-dispersive X-ray spectrometry (EDS), and FIB sample preparation can identify constituent minerals and the microstructures of dust particles (Okada al. 2001; Donarummo et al. 2003; Reid et al. 2003; Gao et al. 2007; Kandler et al. 2007, 2020; Jeong 2008; Conny and Norris 2011; Jeong et al. 2014, 2016; Jeong and Nousiainen 2014; Jeong and Achterberg 2014; Conny et al. 2019).

This paper summarizes the mineralogical and microstructural properties of individual dust particles obtained by electron microscopic analyses and discusses their implications for Earth environments. In particular, I focus on Asian dust migrating to the North Pacific and Saharan dust transported over the Atlantic Ocean, which are important mineral dust on present interglacial Earth and have been previously studied in detail. The paper is written based on microanalytical data obtained at my laboratory over many years using SEM, TEM, EDS, and FIB. Details of experimental methods are also presented.

Applications of SEM and TEM analyses to dust research

SEM analysis of dust particles

Sample preparation and morphological analysis

For SEM analysis, dust particles are collected on polycarbonate membrane filter mounted on suction system (Anderson et al. 1996; Reid et al. 2003), sticky conductive carbon tape attached to the SEM stub on a cascade impactor (Kandler et al. 2007), and cellulose filter on conventional air sampler (Jeong et al. 2014). For cellulose filter, we lightly touch the filter surface with carbon tape to transfer dust particles to the tape. Since individual dust particles are observed, it is necessary to avoid overloading the filter or carbon tape to form thick agglomerates. We should ensure that the dust particles are spaced and evenly distributed by adjusting sampling time according to the atmospheric dust loading and the type of sampler. For electron conduction, dust particles are coated with sputtered metal such as Au, Pt, C, and Os. The Os coating, very thin and coating all sides of the particle, is preferred for the high-resolution and high-contrast imaging because dust particles are typically loose, porous aggregate.

Morphological observation of dust particles is normally performed at an acceleration voltage of ~ 15 kV and a working distance of 15 mm; however, submicron features of the surface are lost under these conditions. High-resolution images of surface features can be obtained at short working distances of less than 10 mm and low acceleration voltages of less than 5 kV.

SEM measures 2D shape parameters of dust particles, such as axial length and circularity (Reid et al. 2003; Gao et al. 2007). The height of the particle can be obtained by the tilting stage (Conny and Norris 2011). The 3D shape of the dust particles can be reconstructed from sequential 2D images obtained by FIB milling (Conny et al. 2020). The cross section of the dust particles exposed by FIB milling can reveal the internal distribution of constituent minerals by EDS mapping (Conny 2013).

Problems with quantitative mineralogical analysis of individual dust particles

Dust particles are commonly classified into chemical types based on EDS data (Maldern et al. 1992; Anderson et al. 1996; Ro et al. 2005; Gao et al. 2007; Conny et al. 2019). However, the mineralogical classification of dust particles has wider implications for the environment (Jeong 2008, 2020; Jeong et al. 2014, 2016; Jeong and Achterberg 2014). The mineralogical classification requires the mineral composition of individual dust particles converted from EDS data. In principle, the quantitative EDS data of a dust particle provide the mineral composition of the particle if we know the chemical composition of constituent minerals. The mineral composition of bulk dust can be obtained from the summation of the mineral compositions of dust particles.

In the real world, however, the interpretation of SEM–EDS data of natural dust particles is complicated due to the irregular morphology, diverse particle size, heterogeneous internal mixing, pores, and varying chemical composition of constituent minerals (Jeong and Nousiainen 2014; Jeong et al. 2016). A chemical composition of thick particles with a flat surface is readily obtained by the SEM–EDS analysis after an established correction procedure for the absorption of emitting X-ray, while the chemical analysis of natural irregular, heterogeneous dust particles using EDS is a challenging issue (Fletcher et al. 2011), and possible only after full characterization of 3D morphology, size, and internal microstructures of dust particles as well as the determination of chemical compositions of constituent minerals, followed by sophisticated correction procedures. Thus, it is practical to treat the EDS data of natural dust particles qualitatively until robust procedures are developed.

Semiquantitative mineralogical analysis of bulk dust

Although it is difficult to determine the mineral composition of an individual dust particle, the mineral species or group dominating the particle can be qualitatively identified from the EDS spectra referring to representative patterns (Figs. 1, 2, 3 and 4), taking into account the heterogeneous mixing of mineral grains (Jeong 2008; Jeong and Nousiainen 2014; Jeong et al. 2016 Supplement). Dust particles are classified and counted based on a predominant mineral species or a mineral group. The particle is counted as 0.5 in the case of the EDS pattern intermediate between two minerals. Summation of the counts leads to the approximate mineral composition of bulk dust. The mineralogical classification of dust particles can determine the mineral composition of a very small amount of dust sample, commonly far below the amount of sample required for quantitative X-ray diffraction (XRD) analysis. To obtain the bulk mineral composition, many particles ($n = 10^3 \sim 10^4$) are analyzed by the assistance of automated SEM–EDS operation (Kandler et al. 2007, 2020; Conny et al. 2019). Manual SEM–EDS analyses can be carried out for a limited number of particles but can resolve ambiguous EDS spectra by quickly adjusting analytical conditions to obtain consistently high-quality spectra. The sorting scheme using the chemical composition of minerals selected from the literature can be applied to the mineralogical classification of dust particles, as done by Donarummo et al. (2003). Such sorting schemes, however, are not satisfactory if we do not know the complex aggregation of minerals in the dust particle and the real chemical composition of each mineral. In addition, the reliability of all SEM–EDS methods to determine the mineral composition of bulk dust should be checked by XRD analysis. Automatic SEM analysis cannot yet replace an analyst's understanding, critical interpretation, and experience in EDS microanalysis problem-solving (Newbury and Ritchie 2013).

TEM analysis of dust particles

TEM specimen preparation

Thin specimens for TEM analysis of minerals have long been prepared by argon ion milling. Currently, TEM specimens are mostly prepared by FIB milling, which is an expensive, complex, but precise method. For FIB milling, we should select target particles representing the mineralogical, chemical, and textural features of the mineral dust (Fig. 1a). Thus, dust particles are preliminarily classified through extensive SEM and EDS surveys based on their size, surface textures, mixing state, chemical composition, and approximate mineral compositions. The selected particles are then milled with a focused gallium ion beam to cut thin lamellae (< 100 nm) (Fig. 1b). Minerals are weak to ion bombardment, which causes amorphization of the lamella surface. The current and acceleration voltage of the ion beam are gradually lowered with thinning of the lamella over several steps to minimize the amorphization of the lamella surface—e.g., 30 kV 3000 pA (lamella thickness 2 ~ 4 μm), 30 kV 500 pA (700 ~ 1000 nm), 30 kV 100 pA (100 ~ 700 nm), 10 kV 50 pA (< 100 nm), 3 kV 10 pA (< 100 nm). Nevertheless, some gallium ions are inevitably implanted into the lamella surface and detected by EDS. Lamellae of small, dense dust particles below 1 μm or less are rather easy to prepare. Preparing lamellae from loose, porous, and irregular dust particles of several μm in size is a challenge (Figs. 1c–d). My experience with several models of FIB instruments managed by dedicated operators shows that successful preparation of high-quality FIB lamellae seems to depend on both instrumental and human factors.

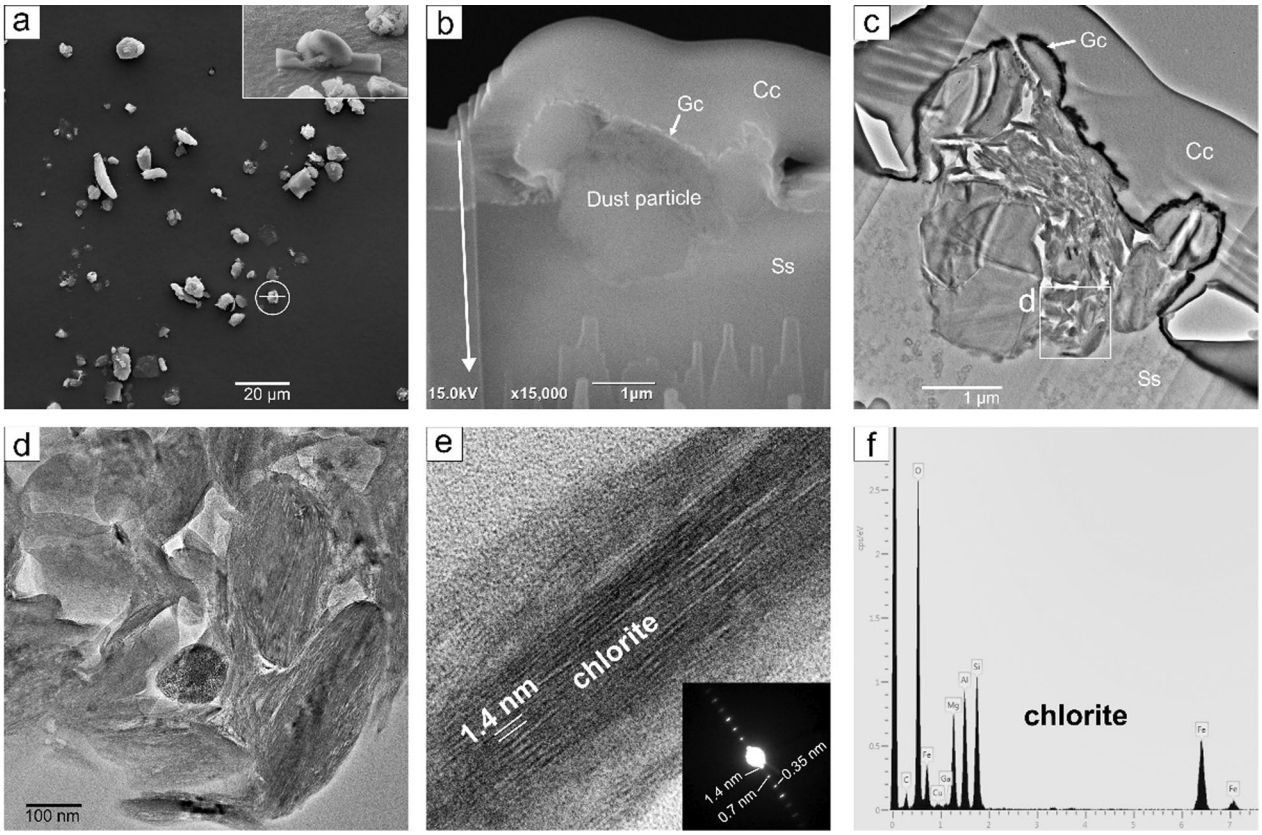

Fig. 1 Preparation of lamellae prepared from dust particles by FIB milling and TEM analysis. **a** Selection of dust particle based on SEM–EDS analyses. Inset shows a deposition of carbon layer on the selected particle. **b** Gallium ion beam milling. SEM image. Arrow indicates the direction of ion beam. **c** Electron-transparent lamella. TEM image. **d** Analyses of internal microstructures. TEM image. **e** Mineral identification by electron diffraction (inset) and lattice imaging. **f** Mineral identification and chemical analysis by EDS. Cc = carbon coating, Gc = gold coating, Ss = substrate (conductive carbon tape). SEM images were obtained at 15 kV using a TESCAN MIRA 3XMH field emission SEM. FIB milling was carried out by a Helios 650 instrument. TEM images were acquired using a JEOL JEM 2010 and a JEOL JEM ARM 200F instruments

Dust particles are aggregates of many mineral grains. The mineral grains dispersed in methanol by ultrasonic agitation are loaded on metal grid covered with a lacey formvar support film. Electron-transparent thin grains are analyzed by EDS and electron diffraction, while electron-opaque large grains and aggregates are not suitable to analysis. This simple, cheap specimen makes it possible to analyze a large number of mineral grains in comparison with the lamella specimen prepared by time-consuming, expensive FIB milling—e.g., chemical analysis of clay minerals in mineral dust (Jeong and Achterberg 2014). However, morphological and microstructural information of dust particles is lost during the sample preparation. Targeted analysis of specific minerals is not easy, compared with FIB lamella because the grains loaded on grid are commonly a mixture of several minerals.

(See figure on next page.)

Fig. 2 SEM images of Asian dust particles acquired at an acceleration voltage of 15 kV and a working distance of 9 mm using a TESCAN MIRA 3XMH field emission SEM. EDS spectra were acquired at 15 kV using an Oxford X-MAX detector. EDS spectra in the energy range of 0.6–5 keV are added on the images. Scale bar = 2 µm. **a** Dust particles collected on cellulose filter using a TSP sampler. **b**–**l** Coarse mineral grains coated with the coatings of micron and submicron clay minerals. Coarse minerals are quartz in (**b**), Na-rich plagioclase (albite) in (**c**), plagioclase in (**d**), K-feldspar in (**e**), illite/muscovite plate in (**f**), biotite plate (**g**). chlorite in (**h**), amphibole in (**i**), calcite in (**j**), dolomite in (**k**), and iron oxide in (**l**). **m** Aggregate of kaolinite. **n** and **o** Aggregate of ISCMs (illite–smectite series clay minerals). **p** Amorphous silica (diatom frustule). **q** Very coarse dust particle. Arrows in (**c**) indicate calcite nanofibers. Arrow in (**o**) indicates gypsum blade. Dust particles in (**a**) were collected in Korea, 16 Mar 2009. Dust particles in (**b**)–(**p**) were collected in Korea, 23 Feb 2015. Dust particle in (**q**) was collected in Korea, 31 Mar 2012

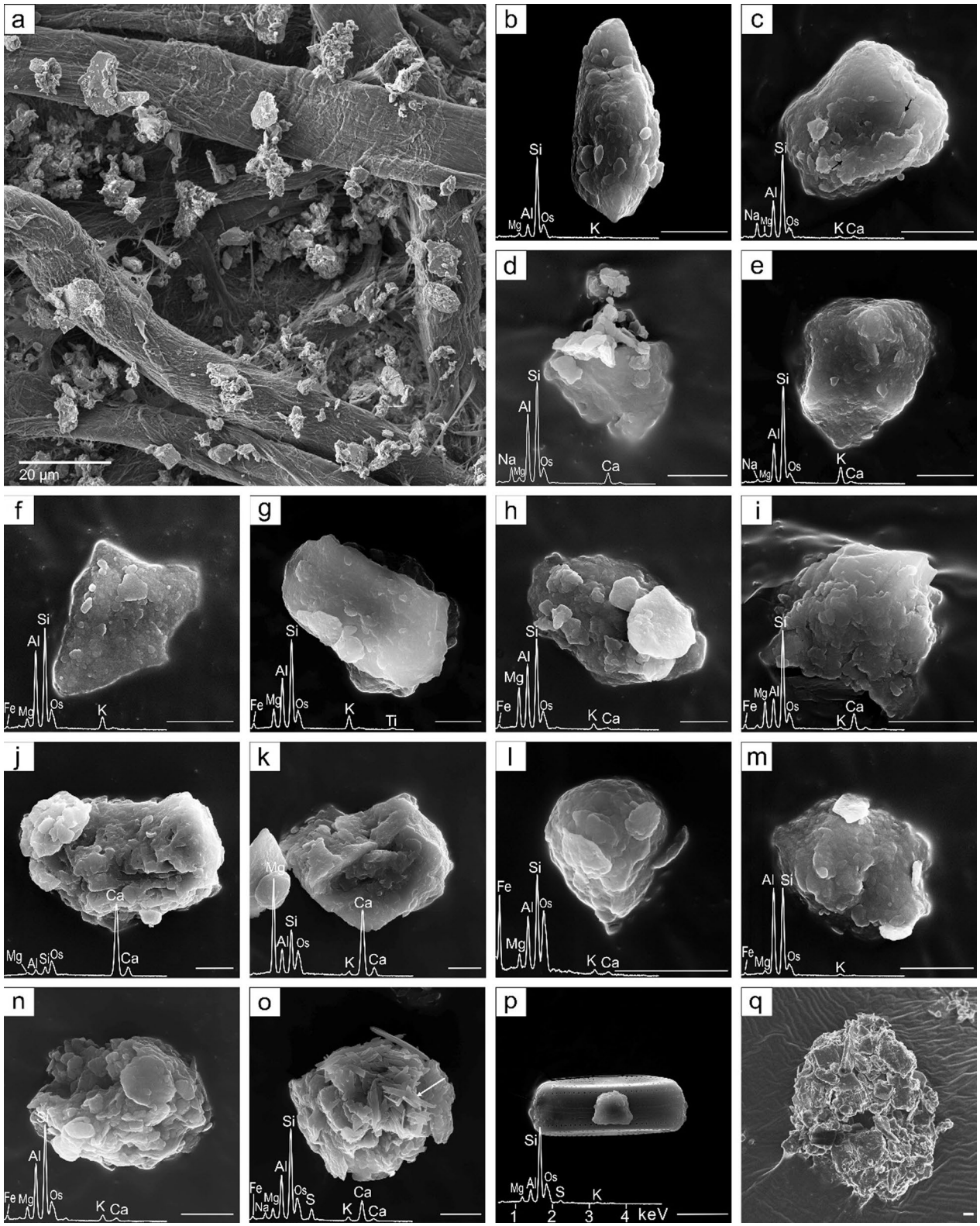

Fig. 2 (See legend on previous page.)

Chemical and microstructural analysis

Minerals in lamellae prepared by FIB are identified by lattice imaging (Fig. 1e), electron diffraction (Fig. 1e), and EDS analyses (Fig. 1f). TEM observations of the lamellae provide rich information on the size, shape, arrangement, and reaction of constituent mineral grains. The thin thickness (< 100 nm) and flat surface of the lamella simplify the quantitative interpretation of characteristic X-rays (Lorimer and Cliff 1976). Elemental compositions are quantified from the EDS spectra by adopting *k* factors derived from the lamellae of mineral standards of known chemical compositions prepared by the FIB technique (Jeong et al. 2016). A major obstacle is severe beam damage when the beam diameter is reduced to analyze submicron mineral grains. The reduction in beam diameter results in the fast degradation of thin lamellae and severe mass loss of alkali and volatile components (Na, K, H_2O, CO_2, and SO_3) included in hydrous clay minerals, carbonates, and sulfates, which are all vulnerable to electron beams. TEM analysts struggle to maintain a balance between the reduction in beam diameter and the minimization of beam damage by adjusting the electron dose and counting time. In my experiences, the minimum beam diameters to analyze common silicate minerals are 50 ~ 100 nm under conventional analytical conditions.

Morphological features of dust particles

Asian dust particles collected by total suspended particle (TSP) samplers in Korea are mostly fine silt up to 20 μm in size (Fig. 2a). They are very fine from a geological viewpoint but rather coarse from an atmospheric point of view. Microscopic hydrous phyllosilicate minerals with layered crystal structures are termed clay minerals. Illite, smectite, chlorite, and kaolinite are generally recognized as common clay minerals in mineral dust, arid soils, and sediments. In the source soils of Asian dust, the submicron platelets of cohesive clay minerals tend to aggregate or adhere on coarse mineral grains to form silty particles (Figs. 3 and 4 of Jeong 2008). Thus, dust particles originating from arid soils and sediments are mostly fine silt particles comprising abundant submicron clay minerals.

Quartz (Fig. 2b), plagioclase (Figs. 2c and d), K-feldspar (Fig. 2e), and calcite (Fig. 2j) are common nonclay minerals with subordinate muscovite (Fig. 2f), biotite (Fig. 2g), chlorite (Fig. 2h), amphibole (Fig. 2i), and dolomite (Fig. 2k). The surfaces of coarse nonclay minerals are covered with submicron platelets of clay minerals. Iron oxides (Fig. 2l) and kaolinite (Fig. 2m) rarely occur as separate aggregates. Illite–smectite series clay minerals (ISCMs including illite, smectite, and interstratified illite–smectite minerals) are the most abundant group of clay minerals forming a clayey aggregate (Figs. 2n and o). Gypsum grains occur as well-developed blades on the surface of dust particles (Fig. 2o) but rarely as coarse grains. Diatom frustules are rare (Fig. 2p). Very coarse dust particles exceeding 20 μm in diameter are commonly complex, loose, and porous aggregates (Fig. 2q). If the particle in Fig. 2q is disaggregated, the daughter particles may be similar to those in Figs. 2b–o.

Nearly all dust particles include ISCMs as major or associated minerals. The EDS spectrum added to Fig. 2n is typical of ISCMs, where the contents of K and Ca vary depending upon the relative abundance of illite and smectite components of ISCMs, respectively. All dust particles include ISCMs, as shown in the weak Mg peaks of quartz, plagioclase, and K-feldspar-rich particles (Figs. 2b–e); K and Si peaks of chlorite-rich particle (Fig. 2h); Al, Si, and K peaks of calcite, dolomite, and iron oxides-rich particles (Figs. 2j–l); and Mg and K peaks of kaolinite-rich particles (Fig. 2m). TEM analyses repeatedly confirmed the common occurrence of ISCMs in dust particles (Jeong et al. 2014; Jeong and Nousiainen 2014; Jeong and Achterberg 2014).

SEM images of Saharan dust particles collected on polypropylene membrane filter using a low-volume sampler (Jeong and Achterberg 2014) are presented in Fig. 3. Saharan dust particles are aggregates of mineral grains of varying sizes (Fig. 3) (Reid et al. 2003; Kandler et al. 2007). Coarse nonclay minerals dominating the dust particles include quartz (Fig. 3a), plagioclase (Fig. 3b and c), K-feldspar (Fig. 3d), muscovite (Fig. 3e), biotite, chlorite (Fig. 3f), calcite (Fig. 3g), dolomite (Fig. 3h), and gypsum (Fig. 3k). Magnified images show that the surfaces of coarse mineral grains are covered with submicron grains of clay minerals. Submicron gypsum blades are scattered on the particle surface (Figs. 3d and h), while coarse

(See figure on next page.)

Fig. 3 SEM images and EDS spectra of Saharan dust particles collected in Cabo Verde, 29 Feb 2008 (Jeong and Achterberg 2014). Images were acquired at an acceleration volatge of 5 kV and a working distance of 7 mm using a TESCAN MIRA 3XMH field emission SEM. EDS spectra were acquired originally in the range of 0–15 keV using an Oxford X-MAXN 50 detector. Bottom image of each panel was magnified from top image. Coarse mineral grains are coated with the coatings of submicron clay minerals. Coarse minerals are quartz in (**a**), plagioclase in (**b**), Na-rich plagioclase (albite) in (**c**), K-feldspar in (**d**), illite/muscovite in (**e**), chlorite in (**f**), calcite in (**g**), dolomite in (**h**), gypsum in (**k**), and palygorskite in (**l**). **i** Aggregate of kaolinite. **j** Aggregate of ISCMs. Arrows in (**d**) and (**h**) indicate gypsum (Gp) blades. Arrows in (a) and (i) indicate hexagonal kaolinite (Kln) plates

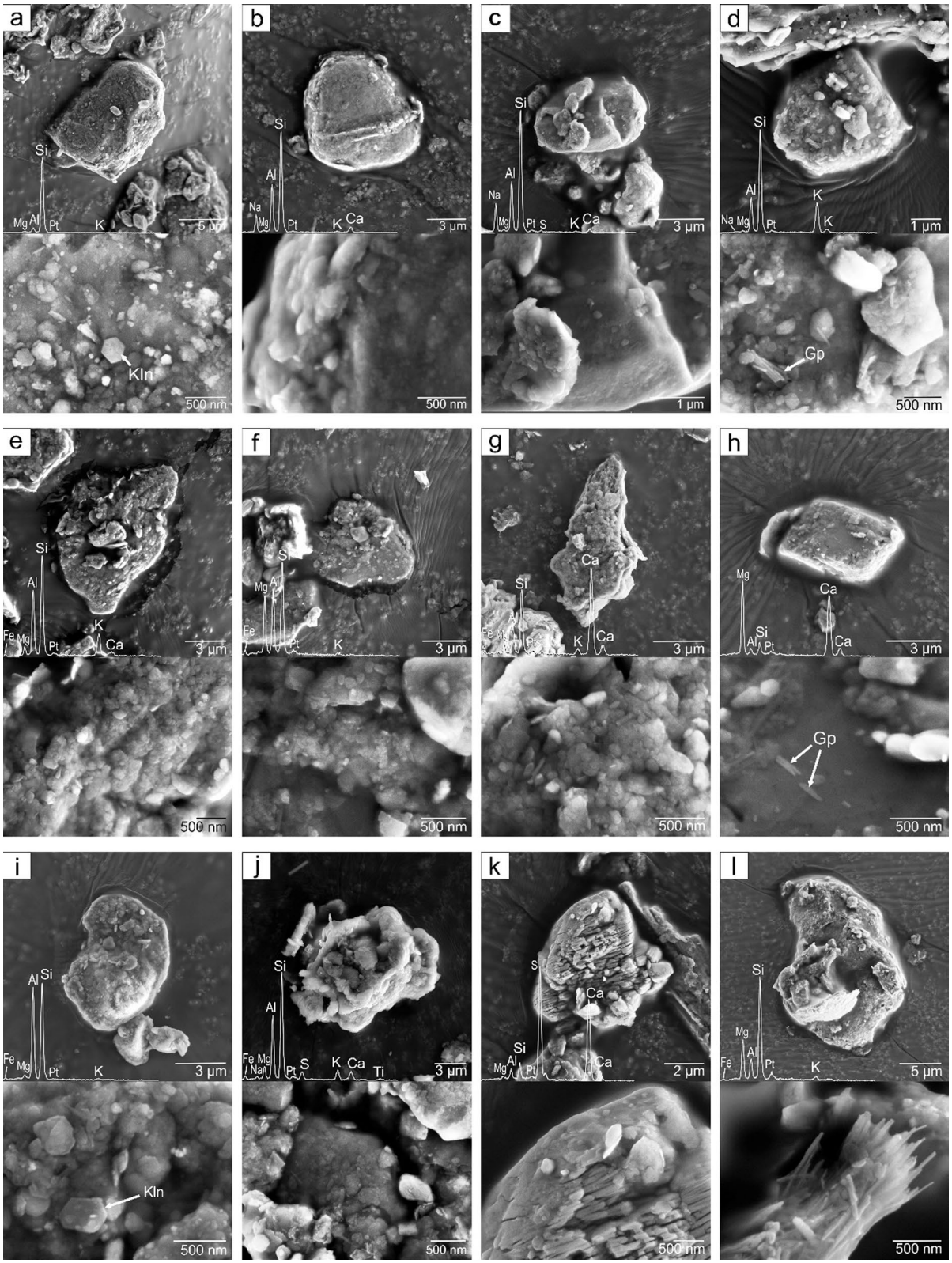

Fig. 3 (See legend on previous page.)

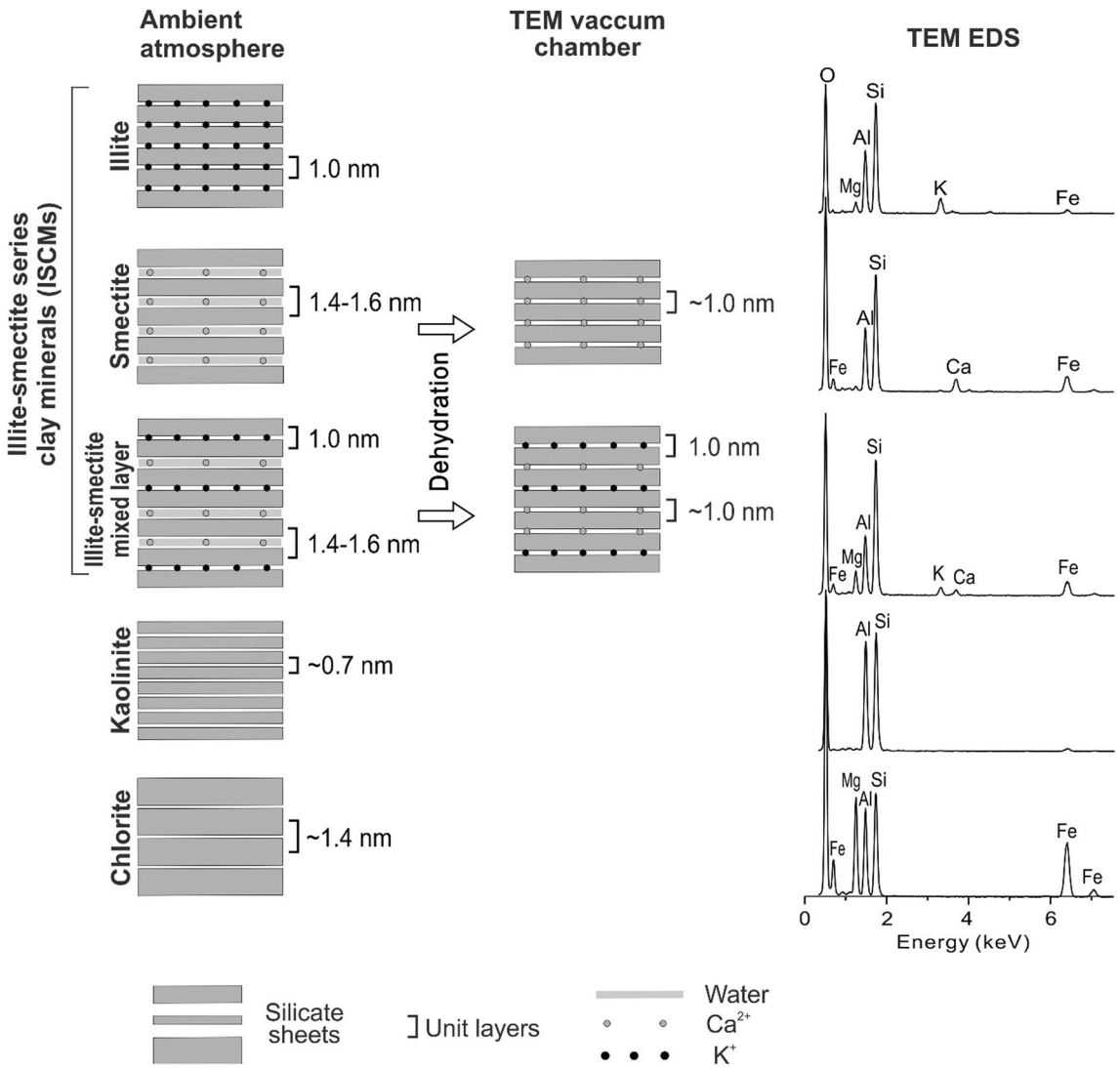

Fig. 4 Structural and chemical features of clay minerals common in dust particles. Stacking of layers in clay minerals is viewed along the crystallographic *a*–*b* plane

gypsum grains have a rounded morphology (Fig. 3k). The clay particles are mostly the aggregates of kaolinite (Fig. 3i) and ISCMs (Fig. 3j). Hexagonal kaolinite plates (Figs. 3a and i) and palygorskite fibers (Fig. 3l) are characteristic of Saharan dust. The EDS spectrum in Fig. 3j is typical of ISCMs in Saharan dust. Almost all Saharan dust particles in Fig. 3 contain ISCMs.

Internal microstructures and mineralogy of dust particles

Phyllosilicates

Basic units of phyllosilicates are silicate layers combining silica-rich tetrahedral sheets and Al–Mg–Fe octahedral sheets in 1:1 and 2:1 ratios. The interlayer is filled with fixed cations or filled with exchangeable cations and H_2O. Phyllosilicates common in both Asian and Saharan dust particles are ISCMs, kaolinite, and chlorite (Fig. 4). TEM lattice fringe imaging and EDS analyses readily identify kaolinite and chlorite, but the clear identification of ISCM group minerals is not easy even by TEM because of the collapse of hydrated smectite interlayer and similar chemical compositions (Fig. 4).

ISCMs

Illite is a nonexpanding, dioctahedral mica-like clay mineral with layer charges of 0.6 ~ 0.85 per $O_{10}(OH)_2$ that are lower than 0.85 ~ 1 per $O_{10}(OH)_2$ of true mica (muscovite and biotite) (Środoń and Eberl 1984; Guggenheim

et al. 2006). The chemical formula of illite is $(K_{0.79}Ca_{0.01})(Al_{1.66}Fe_{0.16}Mg_{0.19})(Al_{0.64}Si_{3.36})O_{10}(OH)_2$ on average based on data in Meunier and Velde (2004). Smectite is an expanding clay mineral with layer charges below 0.6 per $O_{10}(OH)_2$ (Brindley 1980). The chemical formula of smectite is $Ca_{0.21}(Al_{1.55}Fe_{0.13}Mg_{0.33})(Al_{0.16}Si_{3.84})O_{10}(OH)_2$ on average after converting Na to Ca from the data of Na-saturated smectites in Newman (1987). The unit layers of illite and smectite are similar except for interlayer water and cations, thus resulting in common interstratification of illite and smectite layers. The complex interstratification between clay minerals has been extensively documented in soil, sedimentary, and hydrothermal environments (Środoń 1999) but is likely not well recognized outside of the mineralogical community.

The best method to identify interstratified illite–smectite is the simulation of the XRD pattern (Moore and Reynolds 1997). The quantities of samples collected from the long-range transport dust, however, are usually too small to obtain a high-quality XRD pattern required for the simulation. Hence, TEM analysis is alternative approach. Direct lattice imaging may distinguish the illite layer (~1 nm) from the smectite layer (~1.5 nm) in the interstratified illite–smectite. The dehydration of smectite, however, collapses the smectite layer to an ~1 nm layer under the high vacuum of the TEM chamber (Fig. 4), making it difficult to unequivocally identify the illite and smectite layers comprising the interstratified phase (Peacor 1992). Although the direct identification of interstratification is difficult, the K content obtained from ISCMs by EDS analyses can be used as an indicator of illite layers of the ISCMs, because the smectite interlayer is usually saturated with Ca in desert soils and sediments where calcite and gypsum precipitate from evaporating solution.

The cross sections of ISCM-rich particles in Asian and Saharan dust show oriented fabrics composed of parallel to subparallel layers of ~1 nm thickness (Figs. 5a, b, e, 6a, and d). Magnified images show that ISCMs consist of two textural types: 1) compact, straight packets (CSPs) of mottled darker contrast composed of 5–30 layers (Figs. 5a, b, and 6d, e) and 2) loose, curving packets (LCPs) of weak contrast comprising only several layers (Figs. 5a, b, e, 6a, d, and e). Compared with the lattice images of the illitic clays of sedimentary rocks (Ahn and Peacor 1986, 1989), CSPs are illite, while LCPs are likely mixtures of smectite and interstratified illite–smectite. Although some ISCM-rich particles show large internal pores (Fig. 5b), such large pores are rare in clay-rich particles. The subparallel lamella aggregates of ISCMs also coat the coarse mineral grains (Figs. 5c, d, 6d, and e) and fill the intergranular spaces bridging coarse nonclay mineral grains to form composite particles (Figs. 5e, f, and 6f). Aggregates of almost pure smectite, as indicated by high Ca contents, rarely occur in Saharan dust (Fig. 6f) but not in Asian dust.

CSPs occur as thick packets (Figs. 5e, f and 6c) as well as thin packets, while LCPs are always thin. EDS analyses of thick CSPs confirm the chemical composition of illite (Figs. 5e-right, f, and 6c). EDS analyses of LCPs show a variation in K and Ca contents (Figs. 5a, b, e-left, 6a, d, and e), which are interpreted as varying proportions of illite and smectite layers in the analyzed area. K and Fe wt% are quantified from the EDS data of ISCM-rich aggregates and plotted on the scatter diagram (Fig. 7). The chemical compositions of illite, muscovite, and smectite are also plotted for comparison (Newman 1987; Weaver and Pollard 1975; Meunier and Velde 2004). The chemical compositions of pure smectite plot at 0 wt% K, while the compositions of pure illite and muscovite plot above 5 wt% K. Data from ISCMs show varying contents of K. The ISCM data of > 5 wt% K were largely obtained from CSPs that are mostly illite, while the data of < 5 wt% K were mostly from the LCP aggregates. The EDS data of LCPs largely fall between smectite and illite, supporting a common occurrence of interstratified illite–smectite. In Asian dust, LCP data are clustered between 1 and 4 wt% K, while in Saharan dust, data are clustered under 2.5 wt% K. This may indicate that the ISCMs are more illitic in Asian dust, while more smectitic in Saharan dust.

(See figure on next page.)

Fig. 5 TEM images of Asian dust particles acquired at 200 kV using a JEOL JEM 2010 and at 80 kV using a JEOL JEM ARM 200F instruments. EDS spectra were acquired using an Oxford X-MAX detector. Asian dust was collected in Korea, 18 Mar 2014. Inset in top image of each panel is the SEM image of the dust particle obtained just before FIB work. Bottom image of each panel was magnified from the rectangular boxes in top image. EDS patterns were acquired from the circled areas. **a** ISCM-rich particle with goethite (Gth) inclusions. Magnified image shows compact, straight packets (CSPs, illite) of mottled strong contrast scattered through thin loose, curving packets (LCPs, smectite, interstratified illite–smectite) of weak contrast. **b** ISCM-rich particle with circular pore and submicron inclusions of quartz, K-feldspar, chlorite, apatite, barite, and iron oxide. Magnified image shows CSPs scattered through fine LCP matrix. **c** Quartz (highlighted with dashed line) coated with clays. **d** Alkali feldspars (perthite, intergrowth of K-feldspar and albite) coated with ISCM-rich clay. **e** Complex composite particle of clay and nonclay minerals. **f** Composite particle of clay and nonclay minerals. Ab = albite, Afs = alkali feldspars (perthite), Brt = barite, Bt = biotite, Chl = chlorite, Gth = goethite, Ilt = illite, Fo = iron oxide, Kfs = K-feldspar, OM = organic matter, Pl = plagioclase, Qz = quartz. Cc = carbon coating, Gc = gold coating, Ss = substrate (conductive carbon tape)

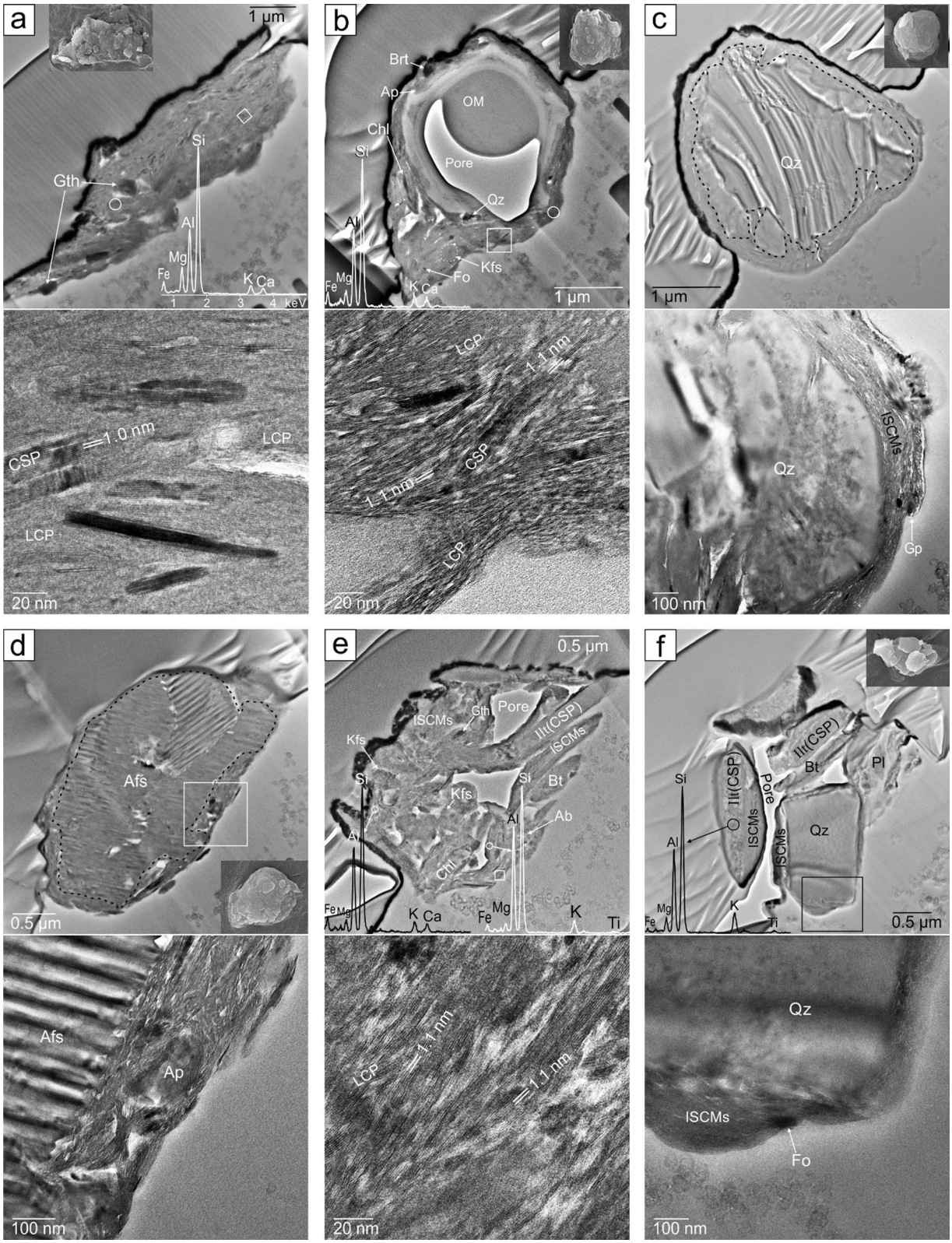

Fig. 5 (See legend on previous page.)

Collective data indicate that LCPs are likely the fine-scale mixtures of interstratified illite–smectite, thin illite (CSPs), and some smectites. We cannot quantitatively split LCPs into illite, smectite, and their interstratified phases. Illite (CSPs) shows a wide range of sizes from nanopackets closely mixed with LCPs to separate platelets. SEM–EDS analyses are poorer even than TEM analyses in discriminating illitic/smectitic clay minerals mixed in the dust particle. Even XRD analysis of a very small amount of dust sample is not straightforward in quantifying illite, smectite, and their interstratified phases. Thus, in the TEM, SEM, and XRD analyses of mineral dust, it is provisionally safe to lump illite, smectite, and interstratified illite–smectite into illite–smectite series clay minerals (ISCMs). Recently, systematic XRD analyses of clays separated from the Mesozoic bedrocks of southern Mongolia which is a major source of Asian dust showed the occurrence of randomly interstratified illite and smectite (Jeong 2022).

Kaolinite, chlorite, micas, and palygorskite

Kaolinite is a 1:1 type phyllosilicate in which one silica tetrahedral sheet is combined with one Al octahedral sheet. Kaolinite [$Al_2Si_2O_5(OH)_4$] can be identified from a 1:1 Al/Si ratio and a lattice fringe of 0.7 nm (Fig. 6a). Submicron kaolinite packets are enclosed in the ISCM aggregates in Saharan (Fig. 6a) and Asian dust (Figs. 2 and 7 of Jeong et al. 2014). Kaolinite is more abundant in Saharan dust than in Asian dust.

Chlorite has a 2:1 type layer structure whose interlayer is occupied by another octahedral sheet. The general formula of chlorite is [$(Mg,Fe,Al)_6(Si_3Al)O_{10}(OH)_8$], in which Mg, Fe, and Al contents vary depending on the geological environment of formation. Chlorite occurs as submicron inclusions in the ISCM-rich clayey aggregates (Fig. 6f of Jeong and Nousiainen 2014) and coarse grains of several microns (Fig. 11 of Jeong and Nousiainen 2014). Chlorite is more abundant in Asian dust.

Micas are mostly biotite and muscovite, which are 2:1 type phyllosilicates whose interlayers are occupied by K. The general formula of biotite is $K(Mg,Fe,Al)_3(Si_3Al)_4O_{10}(OH)_{2,}$ in which the cation numbers of Mg, Fe, and Al vary greatly depending on the geological environment of formation. The average chemical formula of muscovite from Newman (1987) and Deer et al. (1962) is $K_{0.85}(Al_{1.78}Fe_{0.1}Mg_{0.12}Ti_{0.02})_{2.02}(Al_{0.83}Si_{3.17})_4O_{10}(OH)_2$ with little variation. Biotite occurs as submicron grains (Figs. 5e and f) or coarse grains coated with ISCM clays (Fig. 10 of Jeong and Nousiainen 2014; Fig. 4 of Jeong et al. 2016). The high iron content of biotite is comparable to that of chlorite. Muscovite is a coarse phyllosilicate identified by a nearly 1:1 Al/Si ratio and higher K content from illite of a lower Al/Si ratio and lower K content. However, the distinction of fine muscovite from coarse illite is not straightforward when their chemical compositions merge.

Palygorskite occurs as either an aggregate of long fibers or a mixture with other mineral grains in Sahara dust (Figs. 5b and c of Jeong et al. 2016), while it is rare in Asian dust.

Nonphyllosilicates

Quartz is the most abundant nonclay mineral in Asian and Saharan dust. It has globular to ellipsoidal grains of several microns in size coated with ISCM-rich clays (Figs. 5c and 6d) as well as submicron grains enclosed in the ISCM clays (Figs. 5b and 11c). Amorphous silica was identified by electron diffraction and EDS analysis in Saharan dust (Fig. 6e and f) but not in Asian dust. Amorphous silica was a major constituent in three of eight Si-rich dust particles (Tenerife) selected for FIB milling. Thus, the content of amorphous silica should not be overlooked in Saharan dust. SEM–EDS analysis cannot discriminate amorphous silica from quartz.

Feldspars are not only coarse minerals with clay coatings (Fig. 5d; Fig. 7 of Jeong and Nousiainen 2014) but also submicron grains scattered in clay aggregates (Figs. 5b, e, f, 6f, 11c, and d). Feldspars in dust particles include the K-feldspar group (polymorphs of $KAlSi_3O_8$, orthoclase and microcline) and plagioclase group (solid solution series of Na and Ca endmembers ($NaAlSi_3O_8$ and $CaAl_2Si_2O_8$)). The plagioclase group is more abundant than the K-feldspar group (Table 1). Albite is the

(See figure on next page.)

Fig. 6 TEM images of Saharan dust particles acquired at 200 kV using a JEOL JEM 2010 and at 80 kV using a JEOL JEM ARM 200F instruments. Saharan dust was collected with a cascade impactor in Tenerife, 15 July 2005 (Kandler et al. 2007; Jeong et al. 2016). EDS spectra were acquired using an Oxford X-MAX detector. Bottom image of each panel was magnified from top image. EDS patterns were acquired from the circled areas. **a** ISCM-rich particle with interleaved kaolinite packet (0.7 nm lattice). **b** ISCM-rich particle with the submicron inclusions of hematite, goethite, and Ti oxides. **c** Thick illite coated with ISCM-rich clays. **d** Quartz coated with ISCM clays that include submicron goethite and Ti oxide grains. Magnified image shows thin CSPs enclosed in the matrix of LCPs. **e** Amorphous silica coated with ISCM clays. Magnified image shows nano-bubbles of amorphous silica with coatings of CSPs and LCPs. Inset shows diffraction ring of amorphous silica with no diffraction spot. **f** Composite particle of clay and nonclay minerals. Am-Si = amorphous silica, Chl = chlorite, Gth = goethite, Hem = hematite, Ilt = illite, Kfs = K-feldspar, Kln = kaolinite, Sme = smectite, To = Ti oxide, Qz = quartz

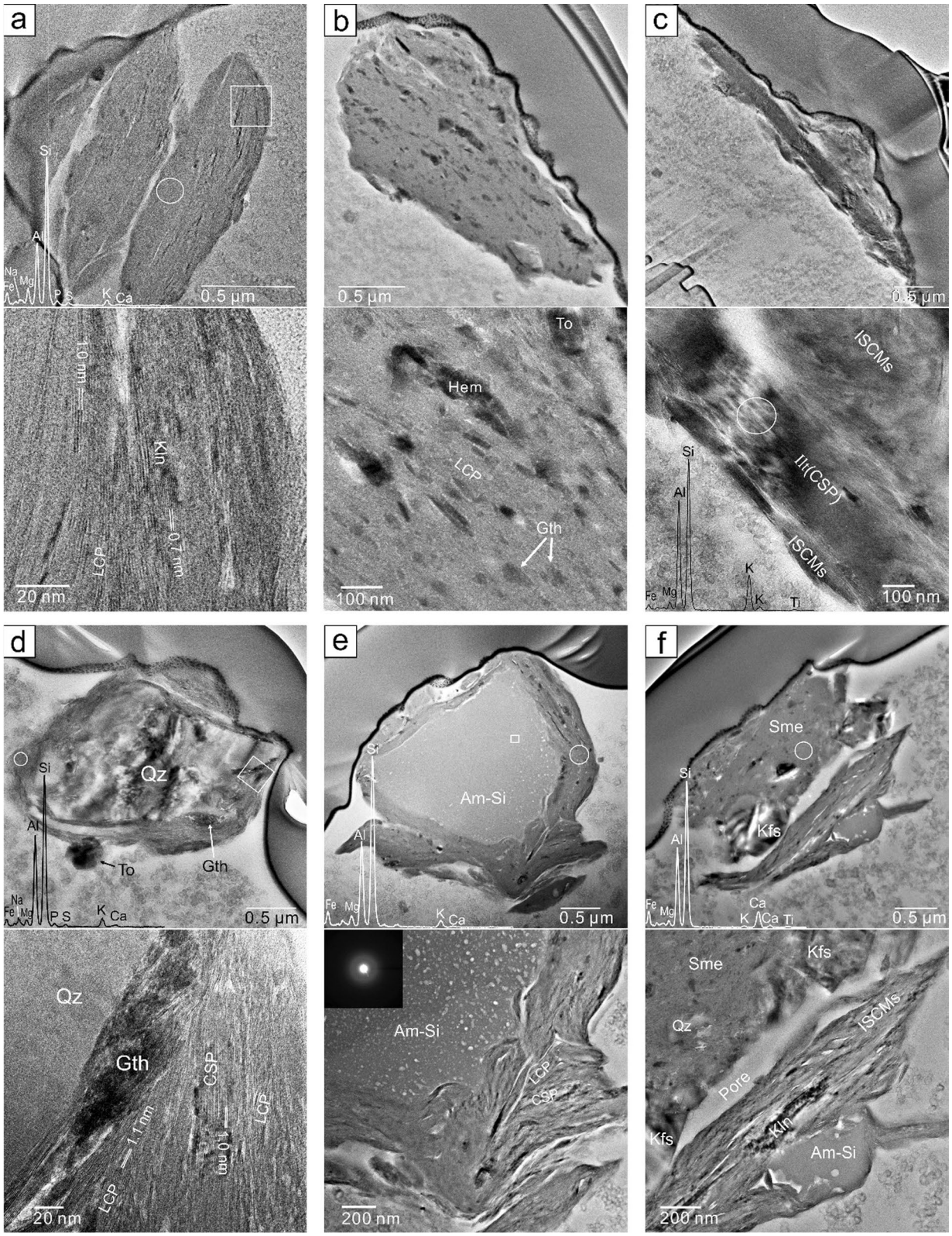

Fig. 6 (See legend on previous page.)

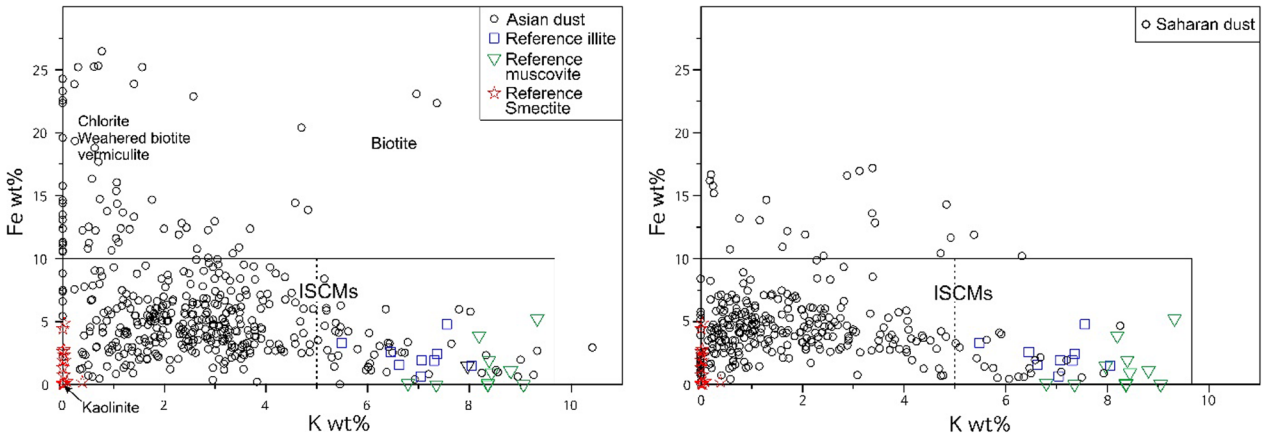

Fig. 7 Scatter plot of Fe wt% vs. K wt% of ISCMs obtained from FIB specimens using an Oxford X-MAX detector installed in a JEOL JEM 2010 TEM. Fe and K wt% were based on 14% H_2O. The box of solid lines indicates the approximate domain of ISCMs. Vertical dashed line separates approximately coarse illite (CSPs) from interstratified illite–smectite, smectite, thin illite, and their mixtures (LCPs). A number of the CSP anlayses are smaller than that of LCP analyses. Data outside the box are those of chlorite, biotite, and their weathering products admixed with ISCMs. Reference illite data from Weaver and Pollard (1975) and Meunier and Velde (2004), muscovite data from Newman (1987) and Deer et al. (1962), smectite data from Newman (1987). Asian dust was collected in Korea, 17 Mar 2009, 31 Mar 2012, and 18 Mar 2014. Saharan dust was collected in Tenerife, 15 July 2005, and in Cabo Verde, 28 Dec 2007–14 Mar 2008

most abundant mineral species in the plagioclase group (Table 1). According to mineralogical analyses of Chinese loess, which is a deposit of Asian dust, 63% of plagioclase grains were albite (Jeong et al. 2008). Albite and K-feldspar also form submicron intergrowths (microperthite) (Fig. 5d).

Amphiboles occur as minor coarse minerals coated with clays in Asian dust (Fig. 9 of Jeong and Nousiainen 2014) but were not detected in Saharan dust.

Calcite and dolomite occur as submicron grains (Fig. 11) and coarse grains with clay coatings (Fig. 8 of Jeong & Nousiainen 2014; Fig. 5b of Jeong et al. 2016). Calcite also occurs as nanofibers (40–50 nm wide) closely associated with ISCMs (Figs. 11a and b; Fig. 2 of Jeong and Chun 2006; Fig. 4 of Jeong et al. 2014). Calcite fibers have not yet been reported in Saharan dust.

Gypsum is common on particle surfaces (Figs. 2o, 3d, and h), while it is scarcely encountered in the interior of dust particles, probably indicating its precipitation on the external surface of dust particles. TEM of some calcite-rich dust particles in Asian dust shows the replacement of gypsum for calcite (Figs. 11c and d).

Iron and titanium oxides are mostly submicron grains scattered through clay aggregates (Figs. 5e, 6b, and d). They appear as rounded to elongated grains of dark contrast in bright field TEM images. Coarse grains of several microns in size are rarely formed (Fig. 12 of Jeong and Nousiainen 2014; Fig. 6 of Jeong et al. 2016). Electron diffraction and lattice imaging characterized goethite, hematite, rutile, and anatase with some magnetite/maghemite.

Microstructures and 3D morphology of dust particles

Three microstructural groups were recognized by the TEM analyses of dust particles (Figs. 8, 9; Fig. 9 and supplement Fig. 2 of Jeong et al. 2016): (1) aggregates of submicron platelets of clay minerals, (2) large nonclay minerals coated with submicron clay aggregates, and (3) composites of clays and nonclay minerals of varying sizes. Of course, there are intergrades among the groups. Fine platelets of ISCMs are arranged subparallel in clay-rich Group-1 particles, resulting in high aspect ratios (Figs. 5a, 6a, b, and 9). The laminae of ISCM platelets coat large nonclay minerals in Group-2 particles (Figs. 5c, d, 6d, e, and 9) and bridge nonclay minerals in Group 3 (Figs. 5e, f, 6f, and 9). The aspect ratios of coarse platy minerals (illite/muscovite, chlorite, and biotite) are very high (Fig. 6c; Fig. 4 of Jeong et al. 2014). The submicron inclusions of quartz, plagioclase, K-feldspar, and chlorite are scattered through clay aggregates. Group-3 particles have commonly irregular pores, while Group-1 and Group-2 particles are less porous. Pore areas of dust particles were measured from the TEM images (Fig. 9) using the lasso tool of Photoshop®. The median porosities of Groups 1($n=14$), 2($n=15$), and 3($n=16$) of Asian dust particles were 2.2, 0.3, and 6.3% in Groups 1, 2 and 3, respectively.

3D shapes of dust particles overall approximate ellipsoids. The lengths of the two axes are measured from 2D SEM images, while the thicknesses of dust particles are obtained as the byproducts of TEM analyses of FIB lamellae (Fig. 9). The average ratios of the three axes are 1.25:1:0.53 in Asian dust (n=45) (Fig. 9) and 1.4:1:0.55

Table 1 Mineral compositions of Asian dust measured by SEM–EDS single-particle and X-ray diffraction analyses (wt%[a])

Sample	Qz[b]	Pl(Ab)	Kfs	ISCMs	Bt	Chl	Kln	Plg	Amp	Cal	Dol	Gp	Fe	Ti	Total clay minerals[c]
Asian dust[d]															
SEM–EDS															
18 Mar 2014 (n = 1096)	18.8	10.7(8.9)[e]	3.6	51.0	0.9	2.7	1.1	0.0	0.8	7.8	0.9	0.4	0.5	0.9	55.7
22–23 Feb 2015 (*n* = 894)[f]	18.8	8.9(8.4)	3.2	52.8	3.0	3.0	2.2	0.0	0.4	4.8	0.3	1.8	0.6	0.2	61.0
6–7 Mar 2016 (n = 824)	16.4	7.5(6.5)	2.5	47.6	1.2	5.4	2.3	0.0	0.7	10.3	2.6	2.3	1.0	0.2	56.5
6–7 May 2017 (n = 470)	18.0	10.9(7.4)	3.4	37.5	3.0	6.8	3.3	0.0	0.2	9.3	0.6	2.4	2.8	1.6	50.6
6–7 April 2018 (*n* = 493)	20.8	9.5(7.6)	4.3	48.5	1.0	4.5	1.5	0.0	1.0	5.4	0.9	1.8	0.3	0.5	55.5
XRD															
18 Mar 2014	17.9	12.3	6.1	47.5	–[g]	3.8	1.3	0.0	1.9	5.5	0.6	3.0	–	–	52.6
22–23 Feb 2015	19.7	10.4	4.2	51.5	–	3.7	2.6	0.0	0.7	3.8	0.3	2.1	–	–	57.8
6–7 Mar 2016	17.4	9.9	4.5	47.4	–	2.8	2.7	0.0	1.2	6.2	1.5	6.4	–	–	53.0
6–7 May 2017	19.9	10.5	4.0	41.3	–	4.4	2.0	0.0	3.8	8.5	2.4	3.3	–	–	47.7
6–7 April 2018	19.0	10.6	6.1	46.4	–	4.8	1.3	0.0	3.0	3.8	1.3	3.6	–	–	52.5
Avg. 25 Asian dusts	20.6	12.4	5.1	42.1	–	4.0	2.1	0.0	1.9	5.1	1.5	5.0	–	–	48.2
Saharan dust															
SEM–EDS															
15 July 2005 (n = 1622)[h]	10.1	2.7(1.8)	2.1	68.0[j]	0.2	1.0	10.9	–	0.1	1.5	0.4	0.7	1.1	1.1	80.1
29 Feb 2008 (n = 612)[i]	11.5	1.9(1.7)	1.9	60.6[j]	0.3	1.1	7.1	–	0.0	9.2	1.6	4.0	0.3	0.4	69.1
XRD[k]															
28–31 Dec 2007	8.8	5.3	1.4	53.4	–	4.8	8.1	4.6	0.0	3.9	1.0	6.1	–	–	70.9
18–23 Jan 2008	12.1	5.5	2.0	50.6	-	4.4	11.0	4.2	0.0	3.0	1.0	4.0	–	–	70.2

[a] Number % obtained by SEM single-particle analyses was converted to weight % on the basis of available data of mineral density

[b] Qz = quartz, Pl = plagioclase, Ab = albite, Kfs = K-feldspar, ISCM = illite–smectite series clay minerals including illite, smectite, and illite–smectite mixed layers, Bt = biotite, Chl = chlorite, Kln = kaolinite, Plg = palygorskite, Amp = amphibole, Cal = calcite, Dol = dolomite, Gp = gypsum, Fe = iron oxides, Ti = titanium oxides. [c]Total clay minerals: sum of ISCM, biotite, chlorite, and kaolinite

[d] Data from Jeong et al. (2020) with the addition of biotite, iron oxides, and titanium oxides. [e]Albite content in parentesis

[f] In Table 2 of Jeong (2020), D18 under title 'Mineral compositions by SEM single-particle analysis' should be repaced by D17

[g] Not determined

[h] Jeong et al. (2016) with the addition of biotite, iron oxides, and titanium oxides. [i]Unpublished data of the author

[j] The higher contents of ISCM in comparison with XRD data are due to palygorskite-bearing samples counted as ISCMs. [k]Jeong and Achterberg (2014). Samples were reanalyzed considering palygorskite content and kaolinite crystallinity

in Saharan dust (n = 48) (supplement Table 1 of Jeong et al. 2016). In Asian dust, clay-rich Group-1 particles are more flattened, whereas other Group-2 and Group-3 particles are more ellipsoidal to spherical (Fig. 9). The aspect ratios of Group-2 particles with mica and chlorite cores are particularly high (Figs. 6c, 8, and 9). The aspect ratios of dust particles are very similar to those measured by the TEM shadow technique in arid regions of China (Okada et al. 2001).

Mineral composition of bulk dust

The bulk mineral compositions measured by EDS analyses are consistent with those determined by XRD (Table 1). Some mismatching between EDS and XRD data is inevitable because minerals with similar chemical compositions are poorly discriminated by EDS analysis, while minerals with similar crystal structures are not distinguished by XRD analysis. Major mineral species and groups are similar in both Asian and Saharan dust. ISCMs are the most abundant mineral group (~ 50%). The equivalents of ISCMs in the previous analyses of Asian dust are the sum of smectite (2%) and illite (49%) (2–20 μm range samples) in Arnold et al. (1998), the sum of smectite (3.1%) and illite (32.7%) in Leinen et al. (1994), and the sum of interstratified illite–smectite and illite (43%) in Shi et al. (2005). The equivalents of ISCMs in Saharan dust are mica (52–65%) in Glaccum and Prospero (1980), the sum of smectite (11.5%) and illite (37%) in Avila et al. (1997), illite (46–54%) in Formenti et al. (2014), illite (49%) in Kandler et al. (2007), and the sum of smectite (32%), illite (6%), and muscovite (7%) in Boose et al. (2016) (Tenerife airborne). The wide mineralogical variation in previous analyses indicates that each study treated differently ISCMs as illite (micas), smectite, or interstratified phases.

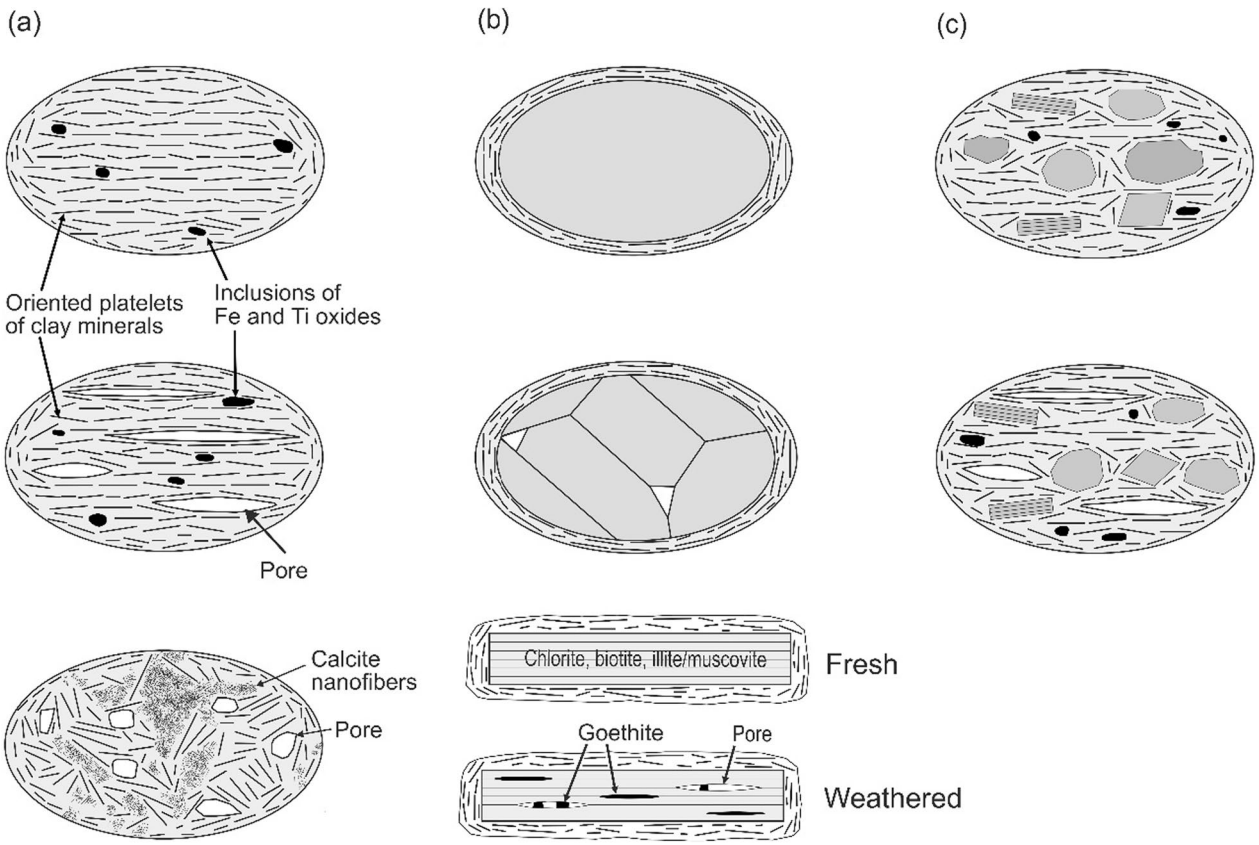

Fig. 8 Models of internal microstructures of dust particles (selected and modified from Jeong and Nousiainen 2014). **a** Aggregates of clay minerals (group 1). **b** Large nonclay minerals coated with clay aggregates (group 2). **c** Composite of clays and nonclay minerals of varying sizes (group 3)

Despite the overall similarity in mineral composition, there are some differences between Asian and Saharan dust. In Saharan dust, the contents of kaolinite and palygorskite are high, while the contents of quartz, plagioclase, and K-feldspar are low in comparison with Asian dust (Table 1). The high contents of kaolinite and palygorskite result in the enhancement of total clay contents in Saharan dust. Amphiboles are present in Asian dust as a minor mineral group but are not detected in Saharan dust. The mineral compositions of Saharan dust vary greatly depending upon the source, reflecting diverse bedrock geology and surface environments (Morinaroli et al. 1996; Ganor and Foner 1996; Avila et al. 1997; Kandler et al. 2007). In any case, ISCMs are the major constituents of Saharan dust.

Dust mineralogy, source geology, and environments

Mineral dust is a link in the global cycle of Earth materials through the lithosphere, pedosphere, atmosphere, and hydrosphere. Dust particles are silty fragments of source soils derived by the weathering of bedrock. All microstructures of the dust particles identified by microanalysis are compatible with those of the source soils (Fig. 4 of Jeong 2008). The mineralogical properties of dust particles discovered through microanalysis provide insight into the geological and soil environments of distant and inaccessible dust sources. Dust particles interact with radiation, atmospheric gas, and liquid. Any interpretation of the interaction should include the mineral composition, crystal chemical properties, and microstructures of the dust particles, improving our understanding of the role of mineral dust in Earth environment.

Phyllosilicates

ISCMs are a dominant mineral group in Asian and Saharan dust. The iron contents of ISCMs cluster at approximately 5 wt%, which is significant because the Fe contents of other major minerals (quartz, feldspars, calcite, and gypsum) are negligible. Dissolution experiments showed that clay minerals were the main source of dissolved iron due to their high solubility (Journet et al. 2008). ISCMs are traced to geologically young sedimentary rocks distributed in desert source areas of Asian and Saharan dust (Graham et al. 2001; Pastore et al. 2021; Jeong 2022). Smectite illitization has been well documented in

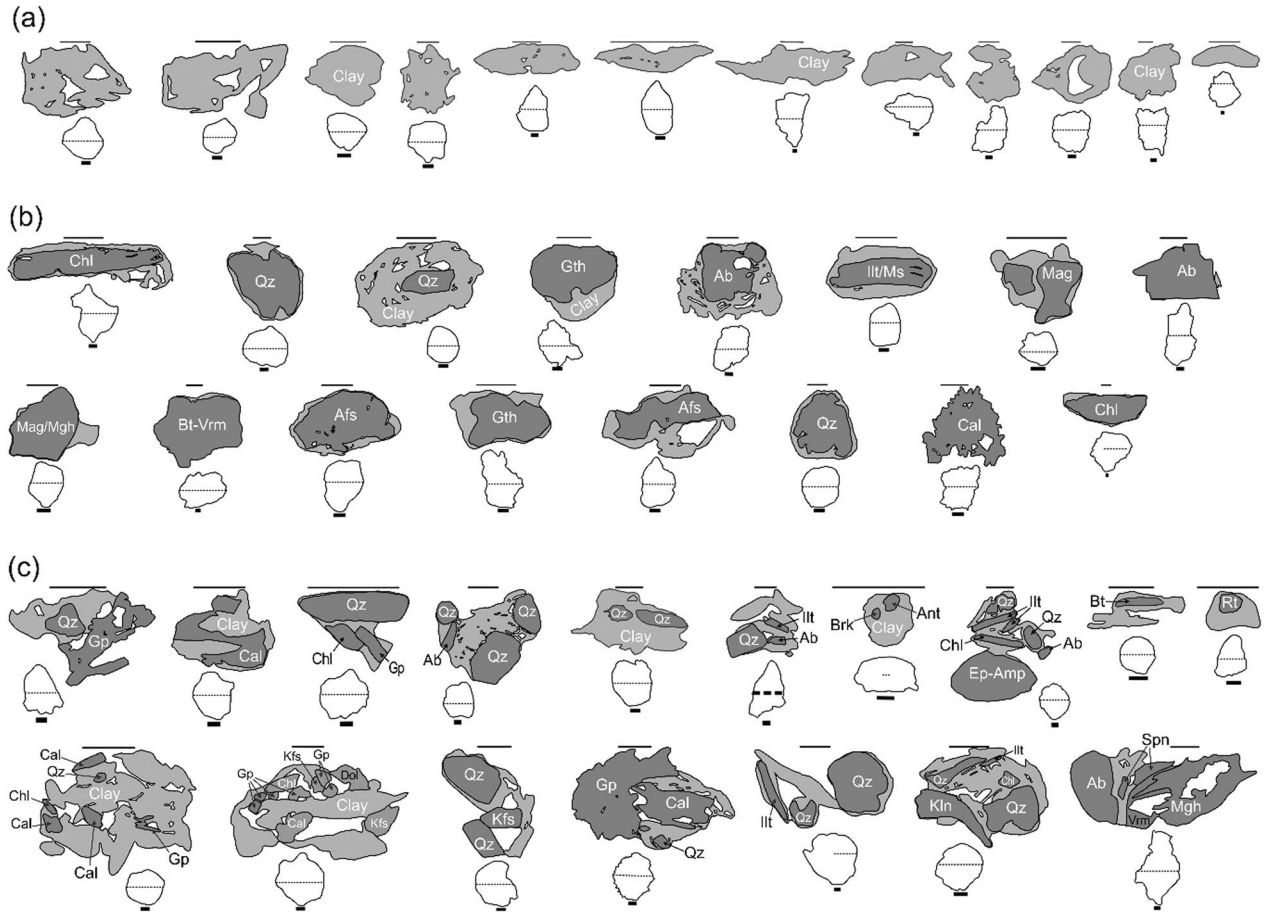

Fig. 9 External shapes and internal microstructures of 45 Asian dust particles collected in Korea, 18 Mar 2014. **a** Aggregates of clay minerals. **b** Large nonclay minerals coated with clay aggregates. **c** Composite of clays and nonclay minerals of varying sizes. Upper drawings: cross sections of the dust particles observed by TEM of FIB lamellae. Lower drawings: outlines of 2D particle shapes observed by SEM (dotted lines are traces of FIB slicing). Thin lines are 1-μm scale bars for FIB sections. Thick lines are 1-μm scale bars for SEM particle shape. White, gray, and dark gray areas of the particles in the upper drawings are pore, aggregates of clay minerals, and nonclay minerals, respectively. Minerals were identified by electron diffraction and energy-dispersive X-ray spectroscopy. Ab = albite, Afs = alkali feldspar (perthite), Amp = amphibole, Ant = anatase, Brk = brookite, Bt = biotite, Cal = calcite, Chl = chlorite, Dol = dolomite, Ep = epidote, Gp = gypsum, Gth = goethite, Ilt = illite, Kfs = K-feldspar, Kln = kaolinite, Mag = magnetite, Mgh = maghemite, Ms = muscovite, Pl = plagioclase, Qz = quartz, Rt = rutile, Spn = sphene (titanite), Vm = vermiculite

sediment diagenesis research (Hower et al. 1976; Lanson et al. 2009; McCarty et al. 2009). Smectite forms during the early diagenesis of siliciclastic sediments, while illite is formed at the later stage of diagenesis via intermediate stages of randomly or regularly interstratified illite–smectite consuming smectite (Hower et al. 1976; Lanson et al. 2009). The mineral assemblage and microtextures observed by TEM in dust particles are comparable to those observed in the diagenetic illitization of smectite (Ahn and Peacor 1986, 1989). Upper Cretaceous to Cenozoic sedimentary bedrocks enriched with illite, smectite, and their mixed layers are widely exposed in the southern Mongolian Gobi Desert, which is the major source of Asian dust (Graham et al. 2001; Jeong 2022). The Sahara Desert is also covered largely with Phanerozoic sedimentary rocks (Pastore et al. 2021).

The chemical composition of kaolinite varies little through diverse geological environments. SEM and TEM images show that the morphologies of kaolinite grains are very different between Asian and Saharan dust. The shape of kaolinite grains in Saharan dust is a hexagonal plate, whereas that in Asian dust is an irregular plate (Figs. 3a, i, and 10), indicating different geological environments in the source areas. Kaolinite in Saharan dust at low latitudes is at least partly the product of ancient lateritic weathering in the southern Sahara and Sahel (Paquet et al. 1984; Caquineau et al. 1998; Goudie and Middleton 2001).

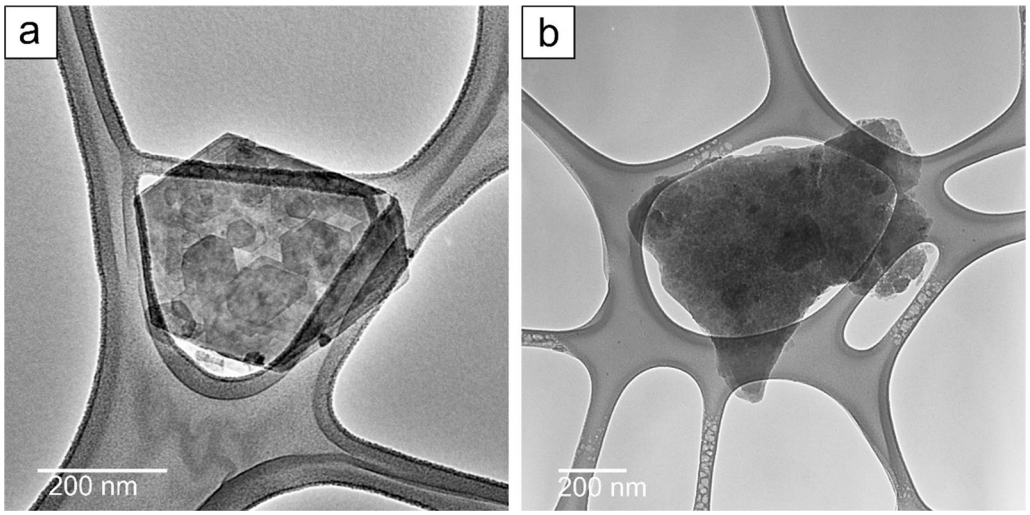

Fig. 10 TEM images of kaolinite grains on lacey carbon grid. **a** Hexagonal platy grain of kaolinite in Saharan dust (29 Feb 2008). **b** Irregular platy grain of kaolinite in Asian dust (27 Mar 2003)

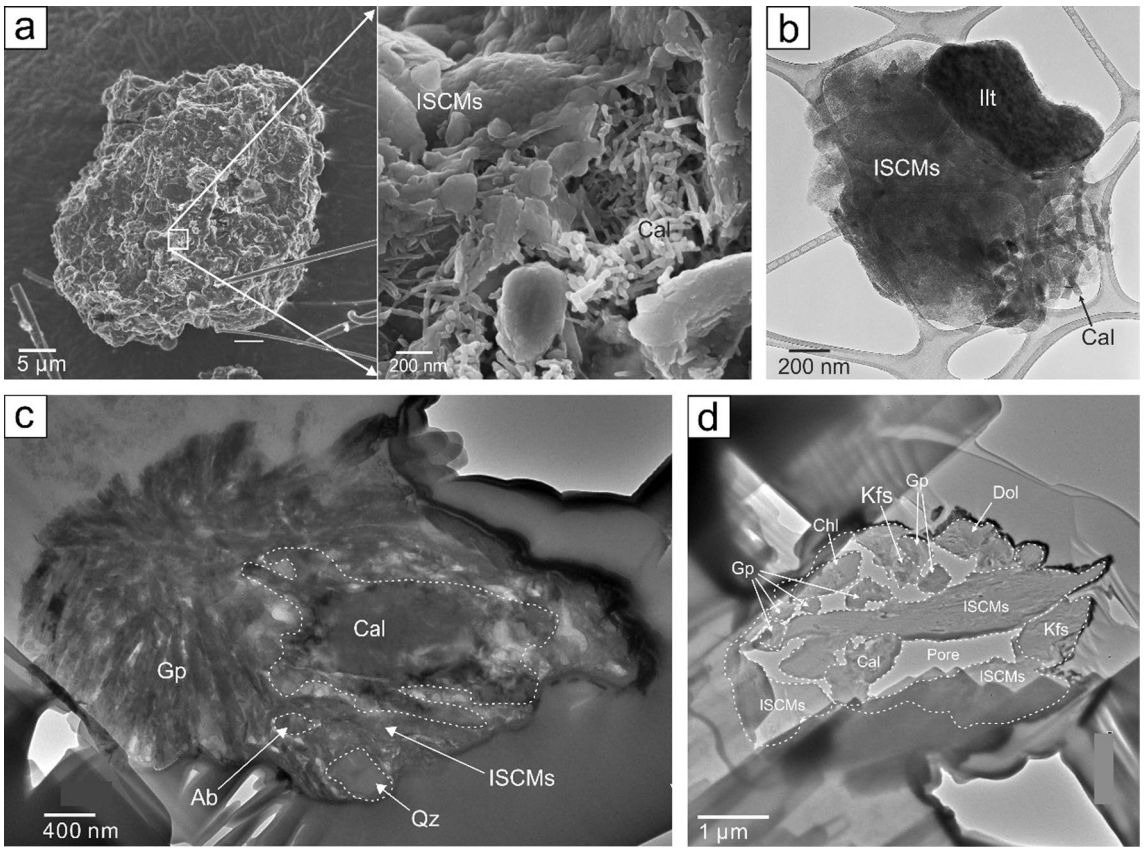

Fig. 11 Calcite in dust particles. **a** Fibrous calcite aggregates filling the cracks of dust particles collected in Korea, 18 Mar 2014. SEM image. Long needles are borosilicate fibers of dust filter. **b** Fibrous calcite mixed with ISCMs and discrete illite in Asian dust (11 Mar 2004). TEM image of particle loaded on lacey carbon. **c** Radiating columns of gypsum replacing calcite in a calcareous Asian dust particle (18 Mar 2014). TEM image of FIB lamella. **d** Gypsum and calcite in a composite Asian dust particle (18 Mar 2014). TEM image of FIB lamella. Ab = albite, Cal = calcite, Chl = chlorite, Dol = dolomite, Gp = gypsum, Ilt = illite, Kfs = K-feldspar, Qz = Quartz

Despite the rather low content in mineral dust, the contribution of chlorite to iron transport is significant due to its high content of structural iron. Reactions with atmospheric acids and clouds increase the iron bioavailability of chlorite by enhancing surface area and precipitating soluble iron compounds (Shi et al. 2012). Pristine chlorite is derived from bedrocks by physical weathering, and partly transformed to vermiculite or interstratified chlorite–vermiculite, precipitating iron oxides by oxidative weathering in soils, (Fig. 11 of Jeong and Nousiainen 2014; Fig. 7e of Jeong et al. 2016). Chlorite was majorly derived from Paleozoic greenschist-facies metamorphism of volcanics and volcaniclastic sediments widely distributed in the sources of Asian dust (Cunningham et al. 2009; Jeong 2022). Diagenetic chlorite, however, may be the major source in Saharan dust.

In sources of Asian dust, the major sources of biotite are Paleozoic grainitic rocks. In soil environments, oxidative chemical weathering transforms biotite to vermiculite and interstratified biotite–vermiculite even in a semiarid climate, precipitating iron oxides (Jeong et al. 2006, 2008, 2011). The low K content and goethite inclusions of some biotite grains (Fig. 10 of Jeong and Nousiainen 2014) indicate chemical weathering in the source area. Muscovite is inherited from igneous, metamorphic, and hydrothermally altered rocks. It is very resistant to chemical weathering and remains in mineral dust without significant chemical and size changes.

Palygorskite $[(Mg,Al)_2Si_4O_{10}(OH)\cdot 4H_2O]$ is a common constituent of Saharan dust (Coude-Gaussen et al. 1987; Molinaroli 1996; Alastuey et al. 2002). Palygorskite is known to form in soils and sediments of arid surface environments in the Sahara (Fedoroff and Courty 1989). Palygorskite was not detected in Asian dust and source soils (Jeong 2020). However, I have detected palygorskite from the XRD analysis of one bedrock (Mesozoic sandstone) sample in the dust source of southern Mongolia.

Other silicates

Quartz (SiO_2) is the most abundant nonclay mineral in mineral dust. It is a major constituent of felsic igneous and metamorphic rocks. Its content is particularly high during coarse dust events (Fig. 4 of Jeong 2020). A fraction of silica in Saharan dust is amorphous silica. The Bodélé depression is known to be the dustiest site in the world, where dust particles originate from diatomite strata composed of biogenic amorphous silica (Todd et al. 2007). However, diatom frustules are rare in the Saharan dust samples collected in the Cabo Verde and the Canary Islands. The bubbles of amorphous silica (Figs. 6e–f) are different from the regularly spaced uniform pores of diatom frustules, indicating that the amorphous silica was formed in source soils from silica-rich solution through changing climates in the Sahara Desert (Gutiérrez-Castorena 2018).

Experiments on ice nucleation highlighted the remarkable efficiency of K-feldspars (Atkinson et al. 2013; Boose et al. 2016; Harrison et al. 2016; Kiselev et al. 2017). K-feldspars, however, are common 'rock-forming minerals' widespread in bedrock and soils. The K-feldspar contents of Asian dust (5%) are not dramatically different from those of Saharan dust (2%) (Table 1). Kandler et al. (2020) showed that K-feldspar abundance measured by SEM–EDS particle analyses was not considerably different among African, Central Asian, and Arctic regimes. Thus, the high ice nucleation efficiency of K-feldspar does not indicate considerable variation in the ice nucleation efficiencies of regional mineral dust. Ice nucleation experiments use freshly exposed surfaces of feldspars, although some experiments treated the surface with acids (Kiselev et al. 2017). Kiselev et al. (2017) showed that epitaxial nucleation on (100) cleavage surfaces of K-feldspar around sharp steps is important for ice nucleation. However, the grains of natural feldspars do not show such clear platy surfaces and sharp steps. In addition, ice nucleation experiments used pure samples. The K-feldspar grains are heterogeneously mixed with numerous mineral grains and tightly covered with aggregates of submicron clay minerals (Figs. 2e, 3d, 5b, d–e; 3c and 5a of Jeong et al. 2016), probably retarding the nucleation and growth of ice crystals. Thus, ice nucleation experiments should be extended to mineralogically well-characterized natural dust.

Amphiboles occur as minor minerals coated with clays in Asian dust (Fig. 9 of Jeong and Nousiainen 2014) but are not found in Saharan dust. Amphiboles were derived by the physical weathering of Paleozoic igneous rocks (andesitic volcanics and amphibole-bearing granitic rocks) and some amphibolite-facies metamorphic rocks in the Mongolian Gobi Desert.

Nonsilicates

Calcite ($CaCO_3$) is a dominant carbonate mineral in both Asian and Saharan dust. Although primary calcite was derived from carbonate and calcareous sedimentary rocks by physical weathering, secondary pedogenic calcite is widespread in arid and desert environments. Fibrous calcite is a form of secondary calcite (Figs. 11a–b) (Verrecchia and Verrechia 1994). Calcite nanofibers were found in the desert soils of western China (Jeong and Chun 2006). Their abundance is generally high in high-carbonate dust originating from calcareous sources, depending upon the migration path of Asian dust storms (Jeong 2020). Calcite nanofibers have not been reported in Saharan dust. However, it is uncertain whether reactive

calcite fibers in Saharan dust may have disappeared due to atmospheric reactions during transport.

Iron and titanium oxides (magnetite, rutile, hematite, and goethite) form either by the weathering of Fe- and Ti-bearing parent minerals or inherit from bedrock. Hematite is a common pigment mineral of reddish sedimentary rocks such as siltstones, sandstones, and conglomerates (Jeong 2022). Significant light absorption by iron oxides in dust has received much attention (Sokolik and Toon 1999; Moosmüller et al. 2012). Lafon et al. (2006) showed that aggregates of iron oxides and clay minerals play an important role in the optical modeling of mineral dust, emphasizing the accurate identification and quantification of iron-oxide mineral species.

Gypsum ($CaSO_4{\cdot}2H_2O$) is a common constituent in both Asian and Saharan dust. Gypsum readily precipitates in evaporating lake sediments. Repeated eolian processes in deserts erode euhedral gypsum crystals of very low hardness to rounded grains. Thus, the rounded coarse gypsum grains in Saharan dust (Fig. 3k) likely originated from a desert source. On the other hand, submicron gypsum in Asian dust (Fig. 2o) resulted from the reaction of calcite with acidic gas in the highly polluted air of heavily industrialized East Asia (Figs. 11c–d). Jeong (2020) showed that gypsum contents have greatly increased in Asian dust in comparison with those in source soils where gypsum content was 0.6 wt% on average (Supplement Table S1 of Jeong 2020). On the other hand, despite no severe industrial pollution, submicron gypsum blades are common on the surfaces of dust particles around the western coast of the Sahara Desert (Figs. 3d and h). Glaccum and Prospero (1980) interpreted gypsum as the reaction product of dust calcite with dissolved SO_4^{2-} during sampling on filters where abundant sea salts were deposited together. Thus, submicron gypsum grains with clear crystal faces in Saharan dust may be related to the marine environments of sampling sites such as Cape Verde (Jeong and Achterberg 2014), Tenerife (Jeong et al. 2016), and Fuerteventura (Coudé-Gaussen et al. 1987).

Asian dust contains diverse rare minerals with a content much less than 1%, such as pyroxene, serpentine, talc, zoisite, epidote, Al_2SiO_5 polymorphs, apatite, Al-phosphate, dolomite, celestine, barite, ilmenite, titanite, and pyrite. Minor minerals have the potential for use as mineral tracers for dust provenance studies (Jeong and Lee 2010). Rare minerals are rare in Saharan dust and deserve further investigation.

Summary

The mineralogy and microstructures of individual dust particles are fundamental to understanding the interactions between mineral dust and Earth environments. The combined application of SEM, TEM, FIB, electron diffraction, and EDS is the best approach to probe the microscopic details of individual dust particles. Electron microscopic analysis of dust particles showed overall similarities and subtle differences between Asian and Saharan dust. Clay minerals are the basic constituents of dust particles, such as clay aggregates, coatings on nonclay minerals, and fine matrices. Their submicron size, platy morphology, high surface area, and cohesiveness control the microstructures and aspect ratios of dust particles. The major clay mineral groups in both Asian and Saharan dust are ISCMs, dominated by illite and interstratified illite–smectite with minor smectite. The mineralogical features of the ISCMs deserve further exploration. Saharan dust is distinguished from Asian dust by the higher contents of hexagonal kaolinite and fibrous palygorskite. The surfaces of nonclay minerals are covered with clay minerals. Freshly exposed surfaces of pure minerals for mineral–atmosphere interaction experiments are different from the natural mineral surfaces of dust particles that experienced long-term weathering and eolian abrasion. The submicron grains of iron oxides and titanium oxides are scattered through the clay matrix of dust particles. The crystal habits of calcite vary widely from massive coarse grains to nanoscale fibrous grains. Submicron euhedral gypsum is an atmospheric reaction product, whereas rounded coarse gypsum originates from a desert source. ISCMs, chlorite, and iron oxides contribute to the delivery of bioavailable iron to remote ecosystems. Electron microscopic analyses characterized the mineralogical details of the Asian dust particles from the Gobi Desert and the Saharan dust particles collected on islands off the western Sahara, while microscopic data are insufficient in the Saharan dust crossing the Mediterranean and originating from the Sahel and other regional dust areas. The climatic role of mineral dust during glacial periods requires the microscopic characterization of ancient dust preserved in eolian deposits around ancient continental ice sheets.

Abbreviations

ISCM	Illite–smectite series clay minerals
SEM	Scanning electron microscopy
TEM	Transmission electron microscopy
EDS	Energy-dispersive X-ray spectrometry
XRD	X-ray diffraction
FIB	Focused ion beam
CSP	Compact, straight packet
LCP	Loose, curving packets

Acknowledgements

The author wishes to thank two anonymous reviewers for their detailed and constructive comments. I would like to thank E. P. Achterberg and K. Kandler for sharing Saharan dust samples.

Author contributions
GYJ obtained and interpreted data, and wrote the manuscript.

Funding
This research has been supported by the National Research Foundation of Korea (Grant no. NRF-2011-0028597 and NRF-2017R1A2B2011422).

Availability of data and materials
All underlying research data are included in this article.

Declarations

Competing interests
The author declares that there are no competing interests.

Received: 9 October 2023 Accepted: 7 March 2024
Published online: 13 March 2024

References

Ahn JH, Peacor DR. Transmission and analytical electron microscopy of the smectite-to-illite transition. Clays Clay Miner. 1986;34:165–79.
Ahn JH, Peacor DR. Illite/smectite from Gulf Coast shales: a reappraisal of transmission electron microscope images. Clays Clay Miner. 1989;37:542–6.
Alastuey A, Querol X, Castillo S, Escudero M, Avila A, Cuevas E, Torres C, Romero PM, Exposito F, Garćia O, Diaz JP, van Dingenen R, Putaud JP. Characterisation of TSP and PM2.5 at Izaña and Sta. Cruz de Tenerife (Canary Islands, Spain) during a Saharan Dust Episode (2002). Atmos Environ. 2005;39:4715–4728.
Anderson JR, Buseck PR, Patterson TL, Arimoto R. Characterization of the Bermuda tropospheric aerosol by combined individual-particle and bulk-aerosol analysis. Atmos Environ. 1996;30:319–38.
Arnold E, Merrill J, Leinen M, King J. The effect of source area and atmopsheric transport on mineral aerosol collected over the North Pacific Ocean. Global Planet Change. 1998;18:137–59.
Atkinson JD, Murray BJ, Woodhouse MT, Whale TF, Baustian KJ, Carslaw KS, Dobbie S, O'Sullivan D, Malkin TL. The importance of feldspar for ice nucleation by mineral dust in mixed-phase clouds. Nature. 2013;498:355–8. https://doi.org/10.1038/nature12278.
Avila A, Queralt-Mitjans I, Alarcón M. Mineralogical composition of African dust delivered by red rains over Northeastern Spain. J Geophys Res. 1997;102:21977–96.
Boose Y, Welti A, Atkinson J, Ramelli F, Danielczok A, Bingemer HG, Plötze M, Sierau B, Kanji JA, Lohmann U. Heterogeneous ice nucleation on dust particles sourced from nine deserts worldwide—Part 1: immersion freezing. Atmos Chem Phys. 2016;16:15075–95.
Brindley GW. Order-disorder in clay mineral structures. In: Brindley GW, Brown G, editors. Crystal structures of clay minerals and their X-ray identification. London: Mineralogical Society; 1980. p. 125–95.
Caquineau S, Gaudichet A, Gomes L, Magonthier M-C, Chatenet B. Saharan dust: clay ratio as a relevant tracer to assess the origin of soil-derived aerosols. Geophys Res Lett. 1998;25:983–6.
Claquin T, Schulz M, Balkanski Y. Modeling the mineralogy of atmospheric dust sources. J Geophys Res. 1999;104:22243–222256.
Conny JM. Internal composition of atmospheric dust particles from focused ion-beam scanning electron microscopy. Environ Sci Technol. 2013;47:8575–81.
Conny JM, Norris GA. Scanning electron microanalysis and analytical challenges of mapping elements in urban atmospheric particles. Environ Sci Technol. 2011;45:7380–6.
Conny JM, Willis RD, Ortiz-Montalvo DL. Analysis and optical modeling of individual heterogeneous Asian dust particles collected at Mauna Loa Observatory. J Geophys Res-Atmos. 2019;124:2702–23. https://doi.org/10.1029/2018JD029387.
Conny JM, Willis RD, Ortiz-Montalvo DL. Optical modeling of single Asian dust and marine air particles: a comparison with geometric particle shapes for remote sensing. J Quant Spectrosc Ra. 2020;254:1–20.
Coudé-Gaussen G, Rognon P, Bergametti G, Gomes L, Strauss B, Gros JM, Le Coustumer MN. Saharan dust on Fuerteventura Island (Canaries): chemical and mineralogical characteristics, air mass trajectories, and probable sources. J Geophys Res-Atmos. 1987;92:9753–71.
Cruz JA, McDermott F, Turrero M, Edwards RL, Martin-Chivelet J. Strong links between Saharan dust fluxes, monsoon strength, and North Atlantic climate during the last 5000 years. Sci Adv. 2021.
Cunningham D, Davies S, McLean D. Exhumation of a Cretaceous rift complex within a Late Cenozoic restraining bend, southern Mongolia: implications for the crustal evolution of the Gobi Altai region. J Geol So. 2009;166:321–33. https://doi.org/10.1144/0016-76492008-082.
Cwiertny DM, Baltrusaitis J, Hunter GJ, Laskin A, Scherer MM, Grassian VH. Characterization and acid-mobilization study of iron-containing mineral dust source materials. J Geophys Res. 2008;113:D05202. https://doi.org/10.1029/2007JD009332.
Deer WA, Howie RA, Zussman J. Rock-forming minerals, Volume 3 sheet silicates. London: Longman; 1962.
Di Biagio C, Balkanski Y, Albani S, Boucher O, Formenti P. Direct radiative effect by mineral dust aerosols constrained by new microphysical and spectral optical data. Geophys Res Lett. 2020. https://doi.org/10.1029/2019GL086186.
Donarummo J Jr, Ram M, Stoermer EF. Possible deposit of soil dust from the 1930's US dust bowl identified in Greenland ice. Geophys Res Lett. 2003;30:1269. https://doi.org/10.1029/2002GL016641.
Fedoroff N, Courty M-A. Indicateurs pedologique d'aridification exemples du Sahara. B Soc Géol Fr. 1989;1:43–53.
Fletcher RA, Ritchie NWM, Anderson IM, Small JA. Microscopy and microanalysis of individual collected particles. In: Kulkarni P, Baron PA, Willeke K, editors. Aerosol measurement. 3rd ed. USA: Wiley; 2011. p. 179–232.
Formenti P, Caquineau S, Desboeufs K, Klaver A, Chevaillier S, Journet E, Rajot JL. Mapping the physico-chemical properties of mineral dust in western Africa: mineralogical composition. Atmos Chem Phys. 2014;14:10663–86. https://doi.org/10.5194/acp-14-10663-2014.
Ganor E, Foner HA. The mineralogical and chemical properties and the behavior of aeolian Saharan dust over Israel. In: Guerzoni S, Chester R, editors. The impact of desert dust across the Mediterranean. Dordrecht: Kluwer Academic Publishers; 1996. p. 163–72.
Gao Y, Anderson JR, Hua J. Dust characteristics over the North Pacific observed through shipboard measurements during the ACE-Asia experiment. Atmos Environ. 2007;41:7907–22.
Glaccum RA, Prospero JM. Saharan aerosols over the tropical north Atlantic—Mineralogy. Mar Geol. 1980;37:295–321.
Goudie AS, Middleton NJ. Saharan dust storms: nature and consequences. Earth-Sci Rev. 2001;56:179–204.
Graham SA, Hendrix MS, Johnson CL, Badamgarav D, Badarch G, Amory J, Porter M, Barsbold R, Webb LE, Hacker BR. Sedimentary record and tectonic implications of Mesozoic rifting in southeast Mongolia. Geol Soc Amer Bull. 2001;113:1560–79.
Guggenheim S, Adams JM, Bain DC, Bergaya F, Brigatti MF, Drits VA, Formoso MLL, Galan E, Kogure T, Stanjek H. Summary of recommendations of nomenclature committees relevant to clay mineralogy: report of the association internationale pour l'Étude des Argiles (AIPEA) nomenclature committee for 2006. Clays Clay Miner. 2006;54:761–72.
Gutiérrez-Castorena del MC. Pedogenic siliceous features. In Stoops G, Marcelino V., Mees F, editors. Interpretation of Micromorphological Features of Soils and Regoliths. 2nd ed. Amsterdam, The Netherlands: Elsevier; 2018. p. 127–155.
Harrison S, Kohfeld KE, Roelandt C, Claquin T. The role of dust in climate changes today, at the last glacial maximum and in the future. Earth-Sci Rev. 2001;54:43–80.
Harrison AD, Whale TF, Carpenter MA, Holden MA, Neve L, O'Sullivan D, Temprado JV, Murray BJ. Not all feldspars are equal: a survey of ice nucleating properties across the feldspar group of minerals. Atmos Chem Phys. 2016;16:10927–40.
Hower J, Eslinger EV, Hower ME, Perry EA. Mechanism of burial metamorphism of argillaceous sediments: 1 Mineralogical and chemical evidence. Geol Soc Amer Bull. 1976;87:725–37.
Huang Y, Kok JF, Kandler K, Lindqvist H, Nousiainen T, Sakai T, Jokinen O. Climate model and remote sensing retrievals neglect substantial

desert dust asphericity. Geophys Res Lett. 2019. https://doi.org/10.1029/2019GL086592.
Jeong GY. Bulk and single-particle mineralogy of Asian dust and a comparison with its source soils. J Geophys Res-Atmos. 2008;113:D02208. https://doi.org/10.1029/2007JD008606.
Jeong GY. Mineralogy and geochemistry of Asian dust: dependence on migration path, fractionation, and reactions with polluted air. Atmos Chem Phys. 2020;20:7411–28.
Jeong GY. Mineralogical comparison between Asian dust and bedrock in southern Mongolia. Korean J Mineral Petrol. 2022;35:397–407.
Jeong GY, Achterberg EP. Chemistry and mineralogy of clay minerals in Asian and Saharan dusts and the implications for iron supply to the oceans. Atmos Chem Phys. 2014;14:12415–28. https://doi.org/10.5194/acp-14-12415-2014.
Jeong GY, Chun Y. Nanofiber calcite in Asian dust and its atmospheric roles. Geophys Res Lett. 2006;33:L24802. https://doi.org/10.1029/2006GL028280.
Jeong GY, Lee K-S. A mineral tracer toward high-resolution dust provenance on the Chinese Loess Plateau: SEM, TEM, and sulfur isotopes of sulfate inclusions in biotite. Amer Mineral. 2010;95:64–72.
Jeong GY, Nousiainen T. TEM analysis of the internal structures and mineralogy of Asian dust particles and the implications for optical modeling. Atmos Chem Phys. 2014;14:7233–54. https://doi.org/10.5194/acp-14-7233-2014.
Jeong GY, Cheong CS, Kim J. Rb-Sr and K-Ar systems of biotite in surface environments regulated by weathering processes with implications for isotopic dating and hydrological cycles of Sr isotopes. Geochim Cosmochim Acta. 2006;70:4734–9.
Jeong GY, Hillier S, Kemp RA. Quantitative bulk and single-particle mineralogy of a thick Chinese loess-paleosol section: implications for loess provenance and weathering. Quaternary Sci Rev. 2008;27:1271–87.
Jeong GY, Hillier S, Kemp RA. Changes in mineralogy of loess-paleosol sections across the Chinese Loess Plateau. Quaternary Res. 2011;75:245–55.
Jeong GY, Choi J-H, Lim HS, Seong C, Yi SB. Deposition and weathering of Asian dust in Paleolithic sites. Korea Quaternary Sci Rev. 2013;78:283–300.
Jeong GY, Kim JY, Seo J, Kim GM, Jin HC, Chun Y. Long-range transport of giant particles in Asian dust identified by physical, mineralogical, and meteorological analysis. Atmos Chem Phys. 2014;14:505–21. https://doi.org/10.5194/acp-14-505-2014.
Jeong GY, Park MY, Kandler K, Nousiainen T, Kemppinen O. Mineralogical properties and internal structures of individual fine particles of Saharan dust. Atmos Chem Phys. 2016;2016(16):12397–410. https://doi.org/10.5194/acp-16-12397-2016.
Journet E, Desboeufs KV, Caquineau S, Colin J-L. Mineralogy as a critical factor of dust iron solubility. Geophys Res Lett. 2008;35:L07805. https://doi.org/10.1029/2007GL031589.
Kandler K, Benker N, Bundke U, Cuevas E, Ebert M, Knippertz P, Rodríguez S, Schütz L, Weinbruch S. Chemical composition and complex refractive index of Saharan mineral dust at Izaña, Tenerife (Spain) derived by electron microscopy. Atmos Environ. 2007;41:8058–74.
Kandler K, Schneiders K, Heuser J, Waza A, Aryasree S, Althausen D, Hofer J, Abdullaev SF, Makhmudov AN. Differences and similarities of Central Asian, African, and Arctic dust composition from a single particle perspective. Atmosphere. 2020;11:269. https://doi.org/10.3390/atmos11030269.
Karydis VA, Tsimpidi AP, Bacer S, Pozzer A, Nenes A, Lelieveld J. Global impact of mineral dust on cloud droplet number concentration. Atmos Chem Phys. 2017;17:5601–21.
Kemppinen O, Nousiainen T, Jeong GY. Effects of dust particle internal structure on light scattering. Atmos Chem Phys. 2015;15:12011–27. https://doi.org/10.5194/acp-15-12011-2015.
Kiselev A, Bachmann F, Pedevilla P, Cox SJ, Michaelides A, Gerthsen D, Leisner T. Active sites in heterogeneous ice nucleation—the example of K-rich feldspars. Science. 2017;355:367–71.
Klein C, Hurlbut CS Jr. Manual of mineralogy. 21st ed. New York: Wiley; 1993.
Kwon H-J, Cho S-H, Chun Y, Lagarde F, Pershagen G. Effects of the Asian dust events on daily mortality in Seoul. Korea Environ Res. 2002;90:1–5. https://doi.org/10.1006/enrs.2002.4377.
Lafon S, Sokolik IN, Rajot JL, Caquineau S, Gaudichet A. Characterization of iron oxides in mineral dust aerosols: implications for light absorption. J Geophys Res. 2006;111:D21207. https://doi.org/10.1029/2005JD007016.
Lanson B, Sakharov BA, Claret F, Drits VA. Diagenetic smectite-illite transition in clay-rich sediments: a reappraisal of X-ray diffraction results using the multi-specimen method. Am J Sci. 2009;309:476–516.
Laskin A, Wietsma TW, Krueger BJ, Grassian VH. Heterogeneous chemistry of individual mineral dust particles with nitric acid: a combined CCSEM/EDX, ESEM, and ICP-MS study. J Geophys Res-Atmos. 2005;110:D10208. https://doi.org/10.1029/2004JD005206.
Leinen M, Prospero JM, Arnold E, Blank M. Mineralogy of aeolian dust reaching the North Pacific Ocean 1. Sampl Anal J Geophys Res-Atmos. 1994;99:21017–23.
Li L, Sokolik IN. The dust direct radiative impact and its sensitivity to the land surface state and key minerals in the WRF-Chem-DuMo model: a case study of dust storms in Central Asia. J Geophys Res-Atmos. 2018;123:4564–82. https://doi.org/10.1029/2017JD027667.
Lorimer GW, Cliff G. Analytical electron microscopy of minerals. In: Wenk HR, editor. Electron microscopy in mineralogy. Berlin: Springer-Verlag; 1976. p. 506–19.
Maldern HV, Rojas C, van Grieken R. Characterization of individual giant aerosol particles above the North Sea. Environ Sci Technol. 1992;26:750–6.
Martin JH, Fitzwater SF. Iron deficiency limits phytoplankton growth in the north-east Pacific subarctic. Nature. 1988;331:341–2.
McCarty DK, Sakhaarov BA, Drits VA. New insights into smectite illitization: a zoned K-bentonite revisited. Am Mineral. 2009;94:1653–71.
McKendry IG, Macdonald AM, Leaitch WR, van Donkelaar A, Zhang Q, Duck T, Martin RV. Trans-pacific dust events observed at Whistler, British Columbia during INTEXB. Atmos Chem Phys. 2008;8:6297–307. https://doi.org/10.5194/acp-8-6297-2008.
Meskhidze N, Chameides WL, Nenes A. Dust and pollution: a recipe for enhanced ocean fertilization. J Geophys Res-Atmos. 2005;110:D03301. https://doi.org/10.1029/2004JD005082.
Meunier A, Velde B. Illite. Berlin, Germany: Springer; 2004.
Middleton N, Yiallouros P, Kleanthous S, Kolokotroni O, Schwartz J, Dockery DW, Demokritou P, Koutrakis P. A 10-year time-series analysis of respiratory and cardiovascular morbidity in Nicosia, Cyprus: the effect of short-term changes in air pollution and dust storms. Environ Health. 2008. https://doi.org/10.1186/1476-069X-7-39.
Mizota C, Endo H, Um KT, Kusakabe M, Matsuhisa Y. The eolian origin of silty mantle in sedimentary soils from Korea and Japan. Geoderma. 1991;49(1–2):153–64.
Molinaroli E. Mineralogical characterisation of Saharan dust with a view to its destination in Mediterranean sediments. In: Guerzoni S, Chester R, editors. The impact of desert dust across the mediterranean. Dordrecht: Kluwer Academic Publishers; 1996. p. 153–62.
Moore DM, Reynolds RC Jr. X-ray diffraction and the identification and analysis of clay minerals. New York: Oxford University Press; 1997.
Moosmüller H, Engelbrecht JP, Skiba M, Frey G, Chakrabarty RK, Arnott WP. Single scattering albedo of fine mineral dust aerosols controlled by iron concentration. J Geophys Res-Atmos. 2012;117:D11210. https://doi.org/10.1029/2011JD016909.
Muhs DR. The geochemistry of loess: Asian and North American deposits compared. J Asian Earth Sci. 2018;155:81–115.
Myriokefalitakis S, Ito A, Kanakidou M, Nenes A, Krol MC, Mahowald NM, Scanza RA, Hamilton DS, Johnson MS, Meskhidze N, Kok JF, Guieu C, Baker AR, Jickells TD, Sarin MM, Bikkina S, Shelley R, Bowie A, Perron MMG, Duce RA. Reviews and syntheses: the GESAMP atmospheric iron deposition model intercomparison study. Biogeosciences. 2018;15:6659–84.
Nesse WD. Introduction to mineralogy. New York: Oxford University Press; 2012.
Newbury DE, Ritchie NWM. Is scanning electron microscopy/energy dispersive X-ray spectrometry (SEM/EDS) quantitative? Scanning. 2013;35:141–68.
Newman ACD. The chemical constitution of clays. In: Newman ACD, editor. Chemistry of clays and clay minerals. London: Mineralogical Society; 1987. p. 1–128.
Nousiainen T. Optical modeling of mineral dust particles: a review. J Quant Spectrosc Ra. 2009;110:1261–79. https://doi.org/10.1016/j.jqsrt.2009.03.002.

Okada K, Heintzenberg J, Kai K, Qin Y. Shape of atmospheric mineral particles collected in three Chinese arid-regions. Geophys Res Lett. 2001;28:3123–6.
Paquet H, Coudé-Gaussen G, Rognon P. Etude minéralogique de poussières sahariennes le long d'un itinéraire entre 19° et 35° de latitude nord. Rév Géol Dyn Géogr. 1984;25:257–65.
Pastore G, Baird T, Vermeesch P, Bristow C, Resentini A, Garzanti E. Provenance and recycling of Sahara Desert sand. Earth-Sci Rev. 2021;216: 103606.
Peacor DR. Diagenesis and low-grade metamorphism of shales and slates. Rev Mineral. 1992;27:335–80.
Pettke T, Halliday AN, Hall CM, Rea DK. Dust production and deposition in Asia and the north Pacific Ocean over the past 12 Myr. Earth Planet Sc Lett. 2000;178:397–413.
Porter SC. Chinese loess record of monsoon climate during the last glacial—interglacial cycle. Earth-Sci Rev. 2001;54:115–28.
Prospero JM. Saharan dust transport over the North Atlantic Ocean and Mediterranean. In: Guerzoni S, Chester R, editors. The impact of desert dust across the mediterranean. Dordrecht: Kluwer Academic Publishers; 1996. p. 133–51.
Reid JS, Jonsson HH, Maring HB, Smirnov A, Savoie DL, Cliff SS, Reid EA, Livingston JM, Meier MM, Dubovik O, Tsay SC. Comparison of size and morphological measurements of coarse mode dust particles from Africa. J Geophys Res. 2003. https://doi.org/10.1029/2002JD002485.
Rex RW, Syers JK, Jackson ML, Clayton RN. Eolian origin of quartz in soils of Hawaiian Islands and in Pacific pelagic sediments. Science. 1969;163:277–9.
Ro C-U, Hwang H, Kim H, Chun Y, Van Grieken R. Single-particle characterization of four "Asian dust" samples collected in Korea, using low-Z particle electron probe X-ray microanalysis. Environ Sci Technol. 2005;39:1409–19.
Scanza RA, Mahowald N, Ghan S, Zender CS, Kok JF, Liu X, Zhang Y, Albani S. Modeling dust as component minerals in the community atmosphere model: development of framework and impact on radiative forcing. Atmos Chem Phys. 2015;15:537–61.
Seinfeld JH, Carmichael GR, Arimoto R, Conant WC, Brechtel FJ, Bates TS, Cahill TA, Clarke AD, Doherty SJ, Flatau PJ, Huebert BJ, Kim J, Markowicz KM, Quinn PK, Russell LM, Russell PB, Shimizu A, Shinozuka Y, Song CH, Tang Y, Uno I, Vogelmann AM, Weber RJ, Woo J-H, Zhang XY. ACE-ASIA regional climatic and atmospheric chemical effects of Asian dust and pollution. B Am Meteorol Soc. 2004;85:367–80.
Shi Z, Shao L, Jones TP, Lu S. Microscopy and mineralogy of airborne particles collected during severe dust storm episodes in Beijing. China J Geophys Res-Atmos. 2005;110:D01303. https://doi.org/10.1029/2004JD005073.
Shi Z, Krom MD, Jickells TD, Bonneville S, Carslaw KS, Mihalopoulos N, Baker AR, Benning LG. Impacts on iron solubility in the mineral dust by processes in the source region and the atmosphere: a review. Aeolian Res. 2012;5:21–42.
Sokolik IN, Toon OB. Incorporation of mineralogical composition into models of the radiative properties of mineral aerosol from UV to IR wavelengths. J Geophys Res-Atmos. 1999;104:9423–44.
Środoń J. Nature of mixed-layer clays and mechanisms of their formation and alteration. Annu Rev Earth Pl Sc. 1999;27:19–53.
Środoń J, Eberl DD. Illite. Rev Mineral. 1984;13:495–544.
Sullivan RC, Moore MJK, Petters MD, Kreidenweis SM, Roberts GC, Prather KA. Effect of chemical mixing state on the hygroscopicity and cloud nucleation properties of calcium mineral dust particles. Atmos Chem Phys. 2009;9:3303–16. https://doi.org/10.5194/acp-9-3303-2009.
Todd MC, Washington R, Martins JV, Duvobik O, Lizcano G, M'Bainayel S, Engelstaedter S. Mineral dust emission from the Bodélé depression, northern Chad, during BoDEx 2005. J Geophys Res. 2007;112:D06207. https://doi.org/10.1029/2006JD007170.
Uno I, Eguchi K, Yumimoto K, Takemura T, Shimizu A, Uematsu M, Liu Z, Wang Z, Hara Y, Sugimoto N. Asian dust transported one full circuit around the globe. Nat Geosci. 2009. https://doi.org/10.1038/NGEO583.
Verrecchia EP, Verrecchia KE. Needle-fiber calcite: a critical review and a proposed classification. J Sediment Res. 1994;64:650–64.
Weaver CE, Pollard LD. The chemistry of clay minerals. Amsterdam: Elsevier; 1975.

Publisher's Note